Modeling of InGaAsSb-Based Avalanche Photodetectors for 2-Micron Wavelengths

Summary of Research

ODURF Project #122231

NASA Grant #NAG-1-02072

Submitted to NASA Langley Research Center

December 2002

Principal Investigator:
Dr. Ravindra P. Joshi

MODELING OF InGaAsSb-BASED AVALANCHE PHOTODETECTORS FOR 2-MICRON WAVELENGTHS

Principal Investigator: Ravindra P. Joshi
Department of Electrical and Computer Engineering
Old Dominion University, Norfolk, VA 23529-0246
(Voice: 757-683-4827 // FAX: 757-683-3220)

NASA Technical Monitor: N. Abedin
Systems Engineering Competency, NASA Langley, Hampton, VA 23681
(Voice: 757-864-4814 // FAX: 757-864-8828)

FINAL REPORT (ODURF # 122231)
December, 2002.

Abstract

The main focus of this research is to study and evaluate the potential of InGaAsSb-AlGaAsSb based 2μm avalanche photo-detectors. The photo-detector contains a separate absorption and multiplication region (SAM) structure. The analysis has mainly been done to understand the electrical response characteristics of the devices existing at NASA, and to evaluate alternate structures proposed. Calculating the current flow for the existing detector structure, on the basis of its energy band diagram, is important. This analysis also helps to find shortcomings in the existing detector structure. It is shown that, unfortunately, the existing structure cannot lead to strong multiplication or voltage dependent gain. Two alternate structures are suggested, that could overcome the inherent flaws, and help achieve improved performance. These devices are obtained through modifications of the original structure, which include varying the doping levels, and changing the thicknesses of detector sub-regions. The results of our study are presented and discussed.

1.1 INTRODUCTION

The main focus of this research is on the potential for 2 μm avalanche photo-detectors based on InGaAsSb-AlGaAsSb, as this material system remains relatively unexplored. The photo-detector contains a separate absorption and multiplication region (SAM) structure. The concept is for InGaAsSb to act as an absorbing region, and for the AlGaAsSb layer to provide for carrier multiplication. The InGaAsSb-AlGaAsSb system is chosen for a variety of reasons. The smaller band gap of (E_g=0.72) of the InGaAsSb relative to the AlGaAsSb (E_g=1.3) region is responsible for absorption in that layer, particularly near the 2 μm [1] wavelength. Due to its large band gap, the AlGaAsSb region will not absorb incident light at this wavelength. Instead, it should act simply as a high-field multiplication region to provide photocurrent gain. The multiplication is based on avalanche multiplication upon the application of a reverse bias voltage to the InGaAsSb-AlGaAsSb diode structure. The present research is aimed at studying the available structures based on the known material parameters and to evaluate device parameters such as dark currents and multiplication, based on a physical device model. Model predictions would then be used for comparisons between predictions and experimental data. Finally, possible device modifications have also been suggested in this report for improving the photodetector response.

1.2 GaInAsSb PHOTODETECTORS

As shown recently, it has become possible to use liquid phase heteroepitaxy of lattice matched GaInAsSb on GaSb substrates to develop mid-infrared detectors. These quaternary alloy systems can provide room-temperature infrared (IR) detectors adjustable for the 1.7-4.5μm range [2]. With proper device design, both the cut-on and cut-off wavelengths can be varied over the range of the quaternary system. A significant advantage of using a quaternary system over the binary and ternary compounds is the ability to vary the band gap while still providing the lattice-matched growth to the substrate material. Another expected advantage is that this detector will have good detectivity at room temperature, while most commercially available detectors need cooling to liquid nitrogen temperatures.

The GaInAsSb/GaSb structure can be fabricated as either a front side or a backside illuminated detector. A diagram of these two designs is shown in figure 1. The GaInAsSb layers can be grown by

liquid phase epitaxy.

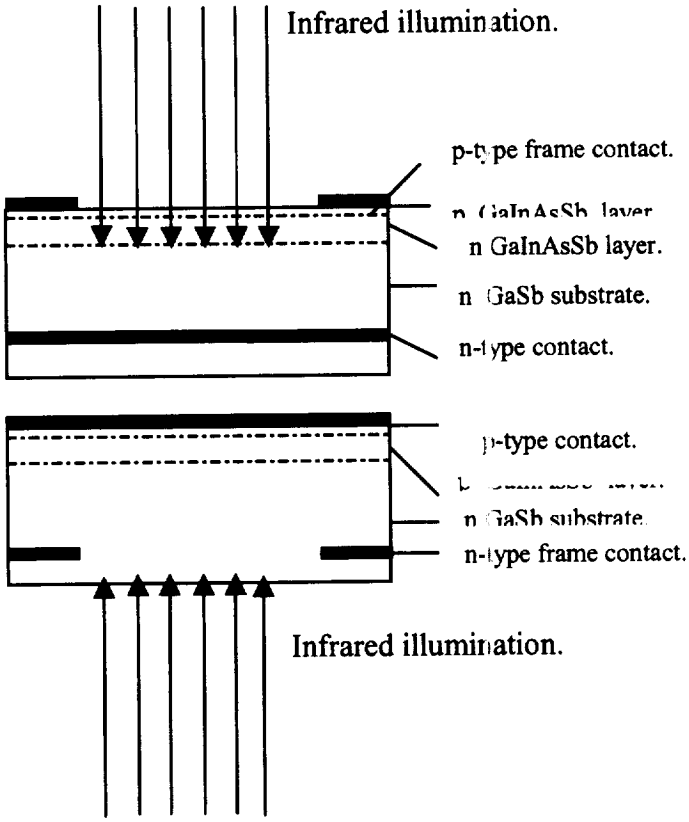

Fig. 1. Front side and backside illuminated detector structures [3].

1.3 REQUIREMENTS FOR A GOOD PHOTO DETECTOR

The main requirements of good avalanche photo-detectors are listed below.

(i) HIGH SIGNAL-TO-NOISE RATIO

An avalanche photo detector is one which can detects the signals that are coming from a source or an object despite their low intensities. The signal coming from the object (for example, from a spacecraft) is typically perturbed by the noise. The noise can be introduced during signal

propagation, or can also be generated by the detector devices and circuits. In order to detect the signal that is largely perturbed by noise, a high signal-to-noise (SNR) ratio detector is desired. A high SNR leads to superior detectibility and increases the threshold level for incoming signals.

(ii) LOW DARK CURRENT

The dark current of a detector is the current that is flowing when there is no photo-excitation. On the other hand, photocurrent is the current when the detector is illuminated by photons. In order to detect the photocurrent with precision, the dark current should be small. Typically, the dark current should be at least an order of magnitude (or more) smaller than the photocurrent for good detection.

(iii) RESPONSIVITY AT DESIRED WAVELENGTHS

A good photodetector must have not only a high signal to noise ratio but also superior responsivity at desired wavelengths. Responsivity is defined as the ratio of the generated photocurrent to the incident signal power. Therefore, the photodetector should yield a maximum response for the desired wavelength range and minimum response for all other wavelengths. This selective property enables the detector to detect particular signal very effectively and efficiently. In the present thesis, the desired wavelength range is around 2 micrometers.

(iv) LARGE PHOTOCURRENT COMPARED TO DARK CURRENT

Photocurrent, the current obtained when the detector structure is illuminated, should be larger in magnitude in comparison with the dark current for correctly distinguishing the difference between them. The photocurrent should be at least an order of magnitude larger than the dark current for better detection.

One way of increasing the detector photocurrent is to engineer internal gain. This can typically be achieved by designing the device such that it can undergo carrier multiplication and internal avalanche action. Under avalanche conditions, large increases in the current can be achieved by very modest increases in the applied voltage. The carrier density typically increases exponentially with both the spatial distance and applied electric field.

(v) HIGH SPEED OF RESPONSE

Another useful requirement is the speed of response. Faster speeds imply a larger operating frequency, and more data can be processed for digital communication and sensing applications.

(vi) LOW DOPING LEVELS

The reduction of doping reduces the dark current as well as the noise in the device because of carrier density reductions in the device. This improves the signal to noise ratio and reduces the detector dark current.

(vii) LOW NOISE

Noise is an unwanted signal that perturbs the detector ability to detect the required signal. The amount of thermal noise present is directly proportional to temperature. Therefore, noise can be reduced by lowering the operating temperature, thereby, suppressing thermal carrier generation. Noise is also dependent on the velocity fluctuations, the amount of generation and recombination in the system, and doping. Lower doping levels and reduced defect levels are both helpful in suppressing noise.

1.4 GAInAsSb AVALANCHE PHOTODIODES

The structure of a GaInAsSb avalanche photo-detector is shown Fig. 2 [4]. The photo-detector consists of n-type InGaAsSb layer that is grown on the n–type Gasb substrate. The InGaAsSb layer acts as an absorbing region because of its small band gap. The n-type AlGaAsSb layer that is grown on the n-type InGaAsSb layer has a band gap that is large when compared to the InGaAsSb because of aluminum composition. This makes it non-absorptive particularly at 2.0 μm wavelengths. A p-type AlGaAsSb layer is grown on the n-AlGaAsSb layer. The p-n AlGaAsSb layer is responsible for the avalanche multiplication upon the application of reverse bias voltage. All the layers are grown by using liquid phase epitaxy and are 3-4 μm thick [5].

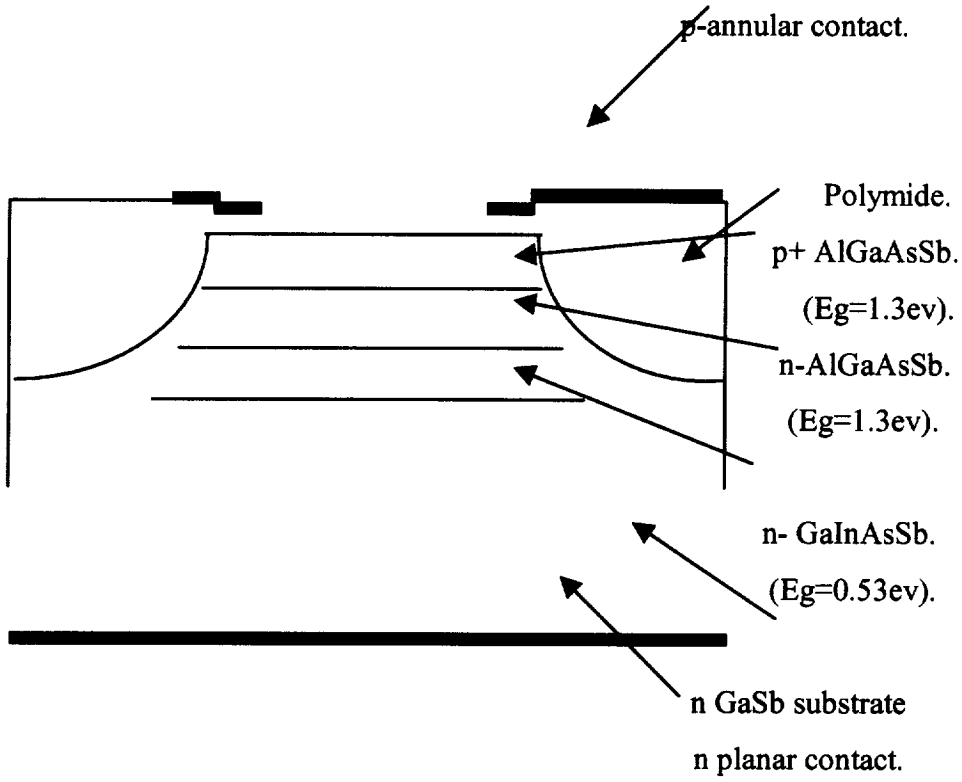

Fig. 2. The IR SAM-APD structure [4].

1.5 ADVANTAGES OF InGaAsSb –AlGaAsSb FOR CURRENT RESEARCH

The selection of InGaAsSb and AlGaAsSb has several advantages over other materials. The potential benefits are stated below:

1. The lower band gap of InGaAsSb is responsible for the absorption particularly at 2μm wavelengths.
2. The larger band gap of AlGaAsSb region is responsible for multiplication and avalanching,

while serving as an optical window.

3. The larger band gap of AlGaAsSb makes it non-absorptive at around 2 μm so the system will act as a separate absorption and multiplication region structure.

2.1 THEORETICAL BACKGROUND

Before proceeding with the analysis and simulation results of the InGaAsSb-AlGaAsSb photodetector system, it is perhaps useful to cover some basic theoretical background. Some of the commonly encountered terms and concepts such as the dark current, avalanche multiplication etc.. are reviewed and presented in the following sections of this report.

2.2 THEORY OF THE DARK CURRENT

In this present discussion, a reverse biased p-n junction with a depletion width of "W" is considered. The electric field "E" can be of arbitrary profile, provided it is sufficiently high in part of the depletion layer to cause impact ionization. It is assumed that the electrons and holes traversing the depletion layer have ionization probabilities per unit length equal to α and β respectively. These ionization probabilities are assumed to be functions of only the electric field E. This means, more precisely, that the ionization probability of an electron or a hole is function of its instantaneous momentum. A carrier moving in a constant electric field will experience a whole spectrum of momentum values, which can be described by a momentum probability distribution for that particular value of E. It is only when it has a momentum value towards the high end of the probability distribution, that it can be capable of an ionizing collision. The assumption that α or β are a function of the local electric field E alone, and not of previous carrier density relies on the following central assumption: The momentum of an individual carrier can sample a large number of values throughout the whole momentum probability distribution within a distance that is small compared to:

1. The mean distance between the ionizing counters, and
2. The distance in which E changes by an appreciable amount.

For example, consider an electron, which has just suffered an ionizing collision so that its

momentum is reduced to near zero. Before it is capable of creating another electron-hole pair, it must gain energy equal to ε_i, the minimum energy (i.e. the threshold value) required for impact ionization. If it gains this energy by moving ballistically through the crystal without collision, gaining energy from the electric field, it will require a distance of ε_i /e*E. Although other methods of gaining energy are possible, the distance ε_i /e*E can be considered as a rough estimate of the distance a carrier needs to have its momentum randomized. The requirement #1 (above) also implies that the total voltage drop across the region in which appreciable ionization occurs must be large compared to ε_i /e. This condition is assumed to be valid throughout this discussion, and generally requires the application of a high device bias. For the sake of simplicity, it is also assumed [6] that recombination within the depletion layer can be neglected, although the equations to be derived can be generalized easily to include it.

2.3 DIODE MULTIPLICATION

Consider a reverse biased avalanche photo-detector in which the high-field region extends from x=0 to x=w as shown in figure 3. In this model the electric field E is taken to be such, that

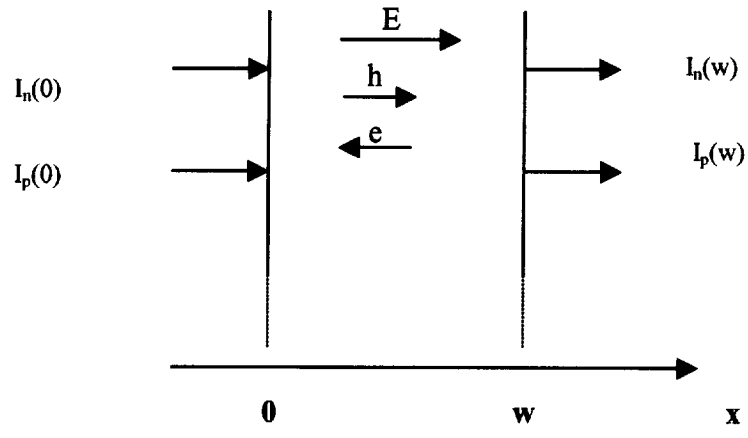

Fig. 3. Schematic diagram of the high-field region of an APD.

the electron drift towards the left and holes to the right. Consider, an electron-hole pair generated

within the depletion region.

In traversing distance dx, the electron will suffer on the average αdx ionizing collisions. Similarly, the hole will create an average of βdx hole-electron pairs as it moves a distance dx. These secondary pairs will themselves start chains of ionizations, the length of each chain depending on where the secondary was created. Thus, if M(x) [7] is the average total number of pairs which are generated in the depletion layer as a result of one initial pair being generated at x, then:

$$M(x) = 1 + \left(\int_0^x \alpha M(x')\,dx'\right) + \left(\int_x^w \beta M(x')\,dx'\right), \qquad (1)$$

where α and β are functions of E which is a function of x'. Differentiating eqn. (1) one gets:

$$\frac{dM(x)}{dx} = (\alpha - \beta) * M(x), \qquad (2)$$

which has a solution,

$$M(x) = M(0)\exp\left[\int_0^x (\alpha-\beta)\,dx'\right].$$

$$= M(w)\exp\left[-\int_x^w (\alpha-\beta)dx'\right]. \qquad (3)$$

Substituting (3) into eqn. (1) for x = w, one obtains

$$M(w) = 1 - \int_0^w \alpha \exp[-\int_x^w (\alpha-\beta)\, dx']\, dx \,. \qquad (4)$$

Therefore, the multiplication factor M(x) is given by:

$$M(x) = \frac{\exp[-\int_x^w (\alpha-\beta)dx']}{1 - \int_0^w \alpha \exp[-\int_x^w (\alpha-\beta)dx']\, dx} \,. \qquad (5)$$

2.4 TOTAL CURRENT

In order to calculate the total current, one can consider the rate at which the electron hole pairs are generated within an element of distance dx. Since holes and electrons are always generated in pairs, only the electrons or the holes (but not both) should be counted. Thus, the pair generation rate results in an increase in the hole current at a location x+dx over the current at position x by an amount $dI_p = (dI_p/dx) * dx.\ dI_p$. This can be expressed as:

$$dI_p = (\alpha I_n + \beta I_p + g)dx \,, \qquad (6)$$

where αI_n is the pair generation rate per unit length due to the impact ionization by electrons, βI_p the rate due to similar collisions by holes, and g is the generation rate per unit length at which the pars are generated either thermally or optically. The value for dI_p/dx can be obtained from the solution of equation (6), and is expressed as:

x

$$I_p(x) = I_p(0)\exp\left[-\int_0 (\alpha-\beta)dx'\right]$$

$$+ \int_0^x (\alpha I+g)\exp\left[-\int_x^w (\alpha-\beta)dx'\right]dx \quad , \qquad (7)$$

where $I = I_p(x) + I_n(x)$ is the total current and is constant. In quasi-steady-state conditions, the total current I is given by:

$$I = I_p(0)*M(0) + I_n(w)*M(w) + \int_0^w g(x)\,M(x)dx \ . \qquad (8)$$

2.5 PHOTO CURRENT

In the present research, as explained earlier, the AlGaAsSb p-n junction acts as a multiplication region and is of particular interest. Assuming that the holes are injected from the left side due to photo excitation and no electrons are injected at x=w the above equation is simplified to:

$$I = I_p(0)*M(0) + I_n(w)*M(w) + \int_0^w g(x)\,M(x)dx\ ,$$

$$= I_p(0)*M(0) + \int_0^w g(x)\,M(x)dx \quad , \qquad (9)$$

since $I_n(w)$ is equal to zero. This assumes that the optical signal is incident from the left, and is at an energy smaller than the AlGaAsSb bandgap. The current in equation (9) is the total current with photo excitation and, therefore, is equal to the photo current. The above expression can be further simplified by assuming α equals β. The expression for M(x) [8] is then simplified as:

$$\exp\left[-\int_x^w (\alpha-\beta)dx'\right]$$

$$M(x) = \frac{x}{1 - \int_0^w \alpha \exp\left[-\int_x^w (\alpha-\beta)dx'\right] dx} .$$

$$= \frac{1}{1 - \int_0^w \alpha(x)\, dx} \quad \text{when } (\alpha=\beta) . \qquad (10)$$

The integral in the equation (9) can also be simplified by assuming a constant generation rate g(x). The expression for g(x) is given by:

$$g(x) = \frac{q*ni*A}{\tau_e} , \qquad (11)$$

where q is the electron charge, ni is the intrinsic concentration, A is the area of the multiplication region and τ_e is the mean electron life time. Substituting (11) and (10) in (9), the photo-current is given by:

$$I = I_p(0)*M(0) + \frac{q*ni*A*w}{\tau_e * \left(1 - \int_0^w \alpha(x)\, dx\right)} . \qquad (12)$$

Since M is independent of x when α equals β, M(0) is same as M(x). Therefore, the above equation can be written as:

$$I_p(0) \qquad\qquad q*ni*A*w$$

$$I = \frac{}{\left(1 - \int_0^w \alpha(x)\,dx\right)} + \frac{}{\tau_e * \left(1 - \int_0^w \alpha(x)\,dx\right)} \quad . \quad (13)$$

2.6 EXPRESSION FOR THE DARK CURRENT

When there is no photo excitation, no holes will be injected into the detector from the x=0 side. Therefore, the dark current is the total current when $I_p(0)$ is zero, and hence the expression for the dark current becomes:

$$I_{dark} = \frac{q*ni*A*w}{\tau_e * \left(1 - \int_0^w \alpha(x)\,dx\right)} \quad . \quad (14)$$

The ratio of photocurrent to the dark current is given by:

$$\frac{I_{photo}}{I_{dark}} = \frac{\left[\dfrac{I_p(0)}{\left(1 - \int_0^w \alpha(x)\,dx\right)} + \dfrac{q*ni*A*w}{\tau_e * \left(1 - \int_0^w \alpha(x)\,dx\right)}\right]}{\dfrac{q*ni*A*w}{\tau_e * \left(1 - \int_0^w \alpha(x)\,dx\right)}} \quad . \quad (15)$$

By simplifying the above expression, one obtains:

$$\frac{I_{photo}}{I_{dark}} = \frac{I_p(0)*\tau_e}{q*ni*A*w}, \quad \text{for } (\alpha = \beta) . \qquad (16)$$

The main aim is usually to increase the above ratio to the maximum extent possible. This can be done by decreasing the depletion width "w" and decreasing the intrinsic concentration n_i. The intrinsic concentration can be reduced by reducing the temperature T because of an inverse exponential dependence on T. Reduction of temperature also reduces thermal noise. Though low temperature operation can benefit the device performance, it comes at the expense of including low-temperature systems. It is thus not a very cost effective procedure, as installing and maintaining the cooling equipment requires a lot of energy and capital.

In general,when α is not equal to β, the ratio of photo current to dark current is given by:

$$\frac{I_{photo}}{I_{dark}} = \frac{I_p(0)*\tau_e*M(0)}{q*A*n_i*\int_0^w M(x)dx} . \qquad (17)$$

Since $M_{avg} = 1/w * \int_0^w M(x)dx$,

$$\frac{I_{photo}}{I_{dark}} = \frac{I_p(0)*\tau_e}{q*A*n_i*w} * \frac{M(0)}{M_{avg}} . \qquad (18)$$

Therefore, attempts to maximize the above ratio M(0) requires a condition, in addition to those stated above. The electric fields have to be maximum at x = 0 and decrease rapidly with x, since the multiplication factor is a monotonically increasing function of the electric field. An electric field that rapidly decays from x=0, will ensure that the corresponding multiplication factor will also decrease.

Thus, the average value will be much smaller than its magnitude at x = 0.

2.7 NOISE CONSIDERATIONS

The noise spectral density within the avalanche photo detector can be calculated by considering the above model. Under the assumption that α and β are functions of E only, the current generated in the element dx should yield the shot noise, given by:

$$< [dI_p - < dI_p >]^2 > = 2*e* dI_p *df , \qquad (19)$$

in an element of bandwidth df. This element of noise current can be thought of as originating from a noise current generator at x and will undergo the same multiplication as any other current generated at x. Thus, if ϕ [9] is the noise spectral density in the total current flowing in the diode, the contribution due to the pair generation rate in dx is given by:

$$d\phi(x) = 2e*M^2(x)\, dI_p(x) . \qquad (20)$$

Integrating one obtains:

$$\phi = 2e\,[I_p(0)* M^2(0) + M^2(w)* I_n(w) + q*A*n_i * \int_0^w dI_p/dx *M^2(x)\, dx] , \qquad (21)$$

where $I_p(0)$, $I_n(w)$ are the thermally and/or optically generated hole and electron currents respectively, entering the two ends of the depletion layer.

The above equation can be further modified by partial integration of the last term. This yields:

$$\int_0^w dI_p/dx *M^2(x)dx = - I_p(0)* M^2(0) + M^2(w)* I_p(w) - 2\int_0^w dI_p/dx *M^2(x)dx. \qquad (22)$$

By rearranging the above equation one can get the final expression for the spectral density. It is given by:

$$\phi = I^* 2^*e^*[\, 2^*\int_0^w \alpha M^2(x)\, dx - M^2(w)] + 4^*e^* I_p(0)^* M^2(0) + M^2(w)^* I_n(w) + 4^*e^* \int_0^w g^* M^2(x) dx \,, \qquad (23)$$

where q is the electron charge, $I_p(0)$and $I_n(w)$ are the hole and electron currents entering the depletion region at x=0 and x=w respectively, g(x) is the rate at which the hole-electron pairs are generated (thermally and/or optically) in the depletion region, and M(x) is the average gain associated with a hole electron pair generated at position x. Provided the values of $\alpha(E)$, $\beta(E)$,and E(x) are known, the above equation can be used to compute the noise spectral density for any desired distribution of injected carriers.

CASE #1:

We consider the case when α is equal to β. When there is no photo excitation $I_p(0)$and $I_n(w)$ are zero. Assuming the g(x) factor [10] is due to thermal excitation, the above equation reduces to:

$$\phi_{da} = 2^*e^*[\, 2^*\int_0^w \alpha M^2(x)dx)\,] + \int_0^w g^* M^2(x)dx * [2^* \int_0^w \alpha M^2(x)dx - M^2(w)] \,, \qquad (24)$$

where ϕ_{da} is the noise spectral density associated with the dark current generated in the region $0 < x < w$. The primary dark current will then be given by:

$$I_{da} = \int_0^w g(x)dx \,. \qquad (25)$$

The mean dark current at the output is given by:

$$(I_{da})_{out} = \int_0^w g(x)\, M(x)dx \quad . \qquad (26)$$

The distributed dark current can be replaced by an equivalent photocurrent source in the p^+ region with the same mean value I_{da}. This can be done by introducing an effective average gain M_{eff}, and an effective noise factor F_{eff}, differing from those for the injected currents, chosen such that $I_{da|out}$ and ϕ_{da} are unchanged. Hence, M_{eff} would be given as:

$$M_{eff} = \frac{(I_{da})_{out}}{I_{da}} \quad . \qquad (27)$$

The above equation can also be written as :

$$M_{eff} = \frac{\int_0^w g(x)\, M(x)dx}{\int_0^w g(x)dx} \quad . \qquad (28)$$

Similarly, the F_{eff} factor would be given by :

$$F_{eff} = \frac{\phi_{da}}{2^* q^* I_{da^*} M^2_{eff}} \quad . \qquad (29)$$

$$F_{eff} = \frac{\left[\int_0^w g(x)dx\right]\left[2*\int_0^w g(x)M^2(x)dx + \left[\int_0^w g(x)M(x)dx\right]*\left[\int_0^w \alpha* M^2(x)*g(x)dx - M^2(w)\right]\right]}{\left[\int_0^w g(x)*M(x)dx\right]^2} \quad . \quad (30)$$

By using the relation $\alpha = \beta$, the F_{eff} factor turns out to be as:

$$F_{eff} = M_{eff} \quad . \quad (31)$$

Consequently, the noise spectral density would then be given by:

$$\phi = 2*q*I_{da}*M^2_{eff} \quad . \quad (32)$$

CASE #2:

If the electron and hole ionization coefficients are not equal, but vary in roughly the same manner with the electric field, then the approximation $\beta = k\alpha$ is reasonable one, with k some fixed constant. With this approximation, the integral in the equation (24) can be performed [11]:

$$2*\int_0^w \alpha M^2(x)dx = 2/(1-k)*\int_0^w (\alpha-\beta) M^2(x)\,dx$$

$$= \frac{M^2(w) - M^2(0)}{1-k} \quad . \quad (33)$$

Therefore, equation (24) becomes:

$$\phi = I*2*e*[k M^2(w) - M^2(0)] + 4*e*I_p(0)*M^2(0) + M^2(w)*I_n(w) +$$

$$\frac{\qquad\qquad\qquad\qquad}{1-k}$$

$$+ \; 4 * e * \int_0^w g * M^2(x)\, dx \,. \qquad (34)$$

In the usual case of interest, most of the ionization occurs over a very short distance that may be only a small fraction of the total depletion width. If a and b represent the locations in the depletion layer of the two ends of the region in which the most ionization occurs, one can write $M(x) \approx M(a)$ for $0 < x < a$, and $M(x) \approx M(b)$ for $b < x < w$. Therefore, the above equation can be written as:

$$\phi = \frac{I * 2*e*[k\, M^2(b) - M^2(a)] \; + \; 4*e*\, I_p(a)*\, M^2(a) + \; M^2(b)*\, I_n(b)}{1-k}$$

$$+ \; 4*e* \int_0^w g \, *M^2(x)dx \;, \qquad (35)$$

$$\text{where } I_p(a) = I_p(0) + \int_0^w g(x)dx \;, \text{ and}$$

$$I_n(b) = I_n(w) + \int_b^w g(x)dx \quad . \qquad (36)$$

The above equation for noise spectral density can be simplified as:

$$\phi = M^3(a)*I_p(a)*[1 + (1-k)*(M(a)-1)^2/k*M^2(a)] +$$

$$+ \; M^3(a)*I_p(a)*[1 - (1-k)*(M(b)-1)^2/M^2(b)]$$

$$+ \; 4*e* \int_b^w g \, *M^2(x)dx$$

$$+\ \frac{k\,M^2(b) - M^2(a)}{1-k} * \int_0^a g * M(x)dx \int_a^w g * M(x)dx \quad . \qquad (37)$$

Here the relationship that M(a)-1 = k(M(b) –1) is used , which is true in the case of $\beta = k\alpha$.

CASE #3:

We now consider the situation where $\beta = k\alpha$ and $M \rightarrow \infty$. For large values of M(b) and M(a) , the M(a) ≈k*M(b) and the last term in the equation is the dominant one. Therefore, ϕ is given by:

$$\phi = 2*e*I*M(a)*M(b)\ , \quad M(a), M(b) \longrightarrow \infty. \qquad (38)$$

This is the spectral density of the current noise generated in the depletion region.

In summary, in the case of $\alpha = \beta$, the noise spectral density is proportional to the third power of the diode multiplication. Since the photodiode signal will be proportional to M, the square of the signal-to-noise ratio will be proportional to $M^2/(2*e*I_t*M^3+\phi_0)$ [12] where ϕ_0 is the equivalent spectral density, referred to the input, of all other noise sources. This will have a maximum for $M = 2*\phi_0 / 2*e*I_t$. If $k\alpha$ is equal to β, roughly the same comments apply. However, the noise spectral density can be greater or less than the $2*e*I_t*M^3$, depending on where the light is absorbed in the junction. If it is absorbed mostly to the left of the high-field region, then the injected current $I_{in} \approx I_t$ and:

$$\phi / 2*e*I_{in} = M^3\,[1+1-k/k*((M-1)/M)^2]\ . \qquad (39)$$

Conversely, if most of I_t originates from light absorbed to the right of the high field region, then $I_{in} \approx I_t$ and:

$$\phi / 2*e*I_{in} = M^3\,[1-(1-k)*((M-1)/M)^2]\ . \qquad (40)$$

Equations are plotted in Figs. 4-5 for various values of k. From the graphs, the following conclusions can be drawn:

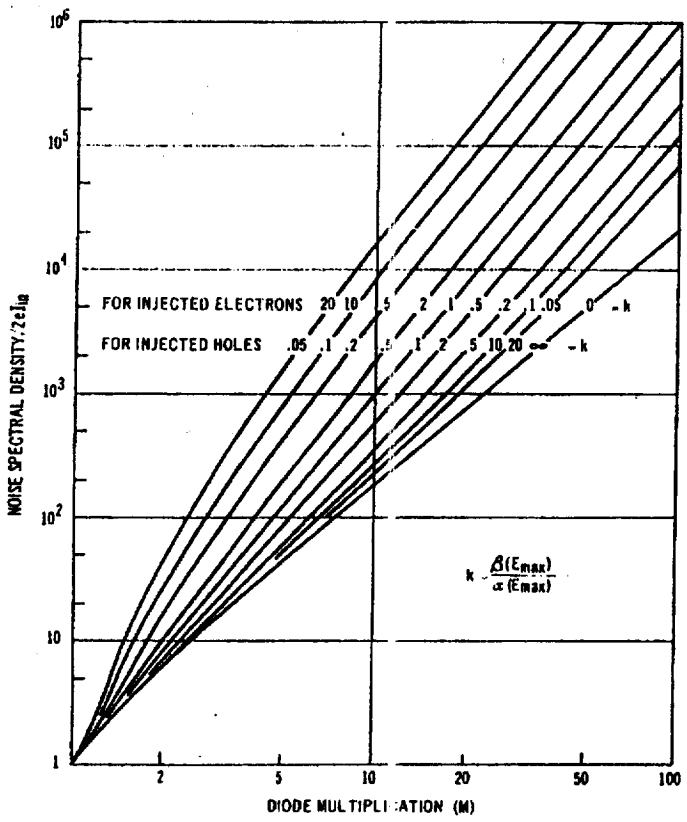

Fig. 4. Noise spectral density/2eI$_{in}$ versus multiplication for either injected holes or electrons if $\beta = K\alpha$.

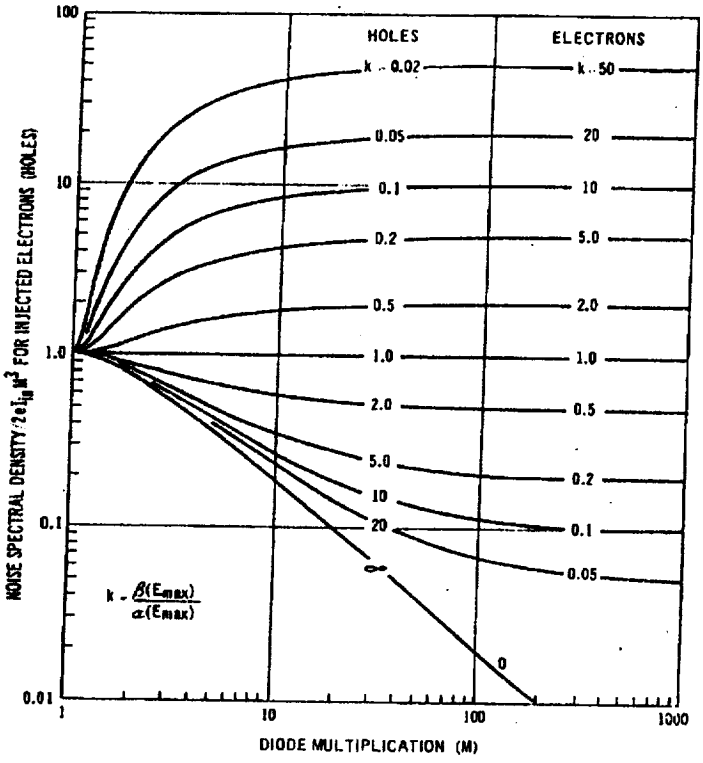

Fig. 5. Noise spectral density/2eI$_{in}$ M ^{3}versus multiplication for either injected holes or electrons if $\beta = K\alpha$.

1. The noise at a given value of M will be less if it can be arranged that most of the carriers entering the high field region are of the more strongly ionizing type.
2. If one wishes to compare the noise measurements made on a real diode with the theoretical curves for $\beta = k\alpha$, k should be considered an adjustable parameter roughly equal to the $\beta(E$ max)/ $\alpha(E_{max})$, where E_{max} is the maximum field in the depletion layer for a given value of M. However, the figure shows that for the more strongly ionizing carrier, F is fairly insensitive to the value of k for low to intermediate values of M. Hence, the theoretical curve for F vs k for large M may be indistinguishable from a plot of experimentally measured values of F vs M. For the less strongly ionizing carrier, on the other hand, F is fairly sensitive to the value of k, so that a single value of k is not expected to give good agreement with experiment, except

when the approximation $\beta=k\alpha$ happens to hold.

Measurements of the hole impact ionization rate in $Al_xGa_{1-x}Sb$ for different compositions [13] is shown in the figure. The fractional alloy composition of As in the $Al_xGa_{1-x}As_ySb_{1-y}$ is 0.08 (i.e. y = 0.08) for the photo-detector structures of interest to NASA. Since the relative composition of As is low, it can be neglected, and therefore, the properties of $Al_xGa_{1-x}Sb$ can nearly be attributed to the actual $Al_xGa_{1-x}As_ySb_{1-y}$. For the given detector, the composition (x) is close to 0.26, for which the $k=(\beta/\alpha)$ ratio is approximately equal to 2.1.

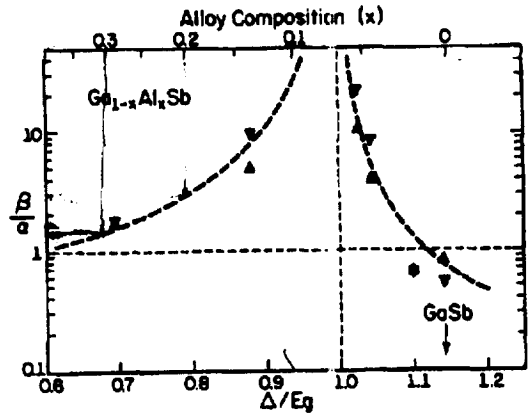

Fig. 6. The variation of $k=(\beta/\alpha)$ with the composition of $Al_xGa_{1-x}Sb$ [13].

3.1 ELECTRIC FIELD CALCULATIONS

Neglecting the GaSb substrate of the photo-detector, the device contains only three regions namely, the n-type InGaAsSb layer, the n-type AlGAAsSb and p-type AlGaAsSb layers as shown in Fig. 7. The energy band diagram (Fig. 8) and the electric field at each point can be calculated at each point by assuming a certain electric field and using Poisson's equation at each junction.

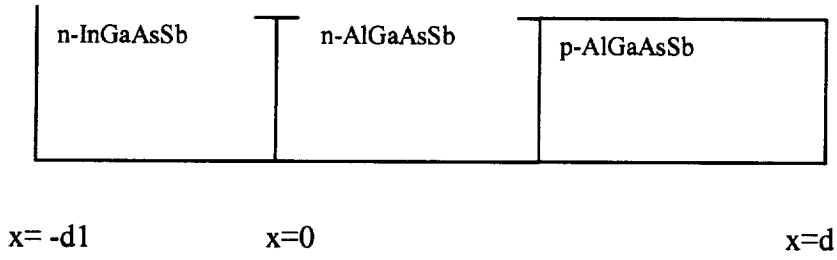

Fig. 7. The structure of avalanche photo detector.

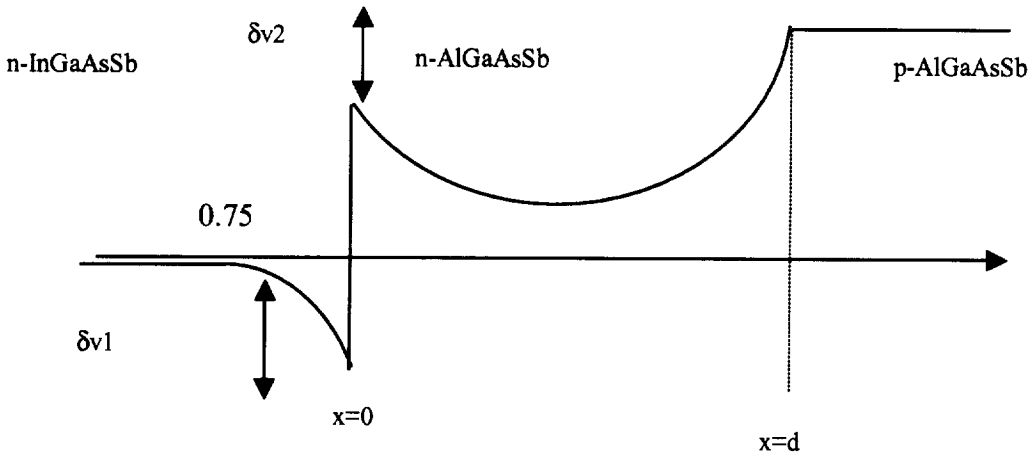

x =-d1

Fig. 8. The expected energy band diagram of the above detector.

The electric field at $x=0^+$ is assumed to be a value equal to E0. The electric field can be positive or negative. Here, two cases have been considered, one with a positive electric field and another with negative electric field. The equation governing the two junctions is expressed as:

$$-\delta e1-\delta v1+0.75\ -\delta v2-E_{g2}-\ \delta e2\ =Va, \tag{41}$$

where $\delta e1$ is the energy gap between the conduction band and Fermi level in InGaAsSb and $\delta e2$ is the energy difference between the valence band and Fermi level in p-AlGaAsSb. The parameters $\delta v1$ and $\delta v2$ are the voltages developed in the two junctions, while 0.75 represents the band offset between n-InGaAsSb and n-AlGaAsSb, and E_{g2} is the band gap of AlGaAsSb. This equation is derived from the continuity of energy across the entire device, and is valid for a given applied voltage Va.

CASE #1: The procedure for evaluation of the electric field profile and voltage distribution within the device is described in this section. This procedure has been used throughout this thesis for calculations of the energy band diagrams. For concreteness, we begin by assuming that the initial electric field E0 is greater than zero, and the voltage $\delta v1$ is negative. Use is made of the governing equation is the Poisson equation. Not only E0, but also a negative value of $\delta v1$, is assumed. By applying Poisson's equation for x less than zero:

$$dE/dx=\ q^*[Nd_{\ InGaAsSb}\ -n(x)]/\ \varepsilon_{\ InGaAsSb}\ , \tag{42}$$

where n(x) is the carrier density for x less than zero. The electric field is varied according to the above equation with respect to x by incrementing x in small steps with a starting value at x=0. The initial value of the electric field can be obtained from the continuity of D (the electric flux density):

$$E(0^-) = \varepsilon_{\ InGaAsSb}{}^*E0\ /\varepsilon_{\ AlGaAsSb}\ . \tag{43}$$

The initial value of carrier density can be calculated from the formula:

$$n(0)=nd1*\exp((q*\delta v1)/(kb*T)) \quad . \qquad (44)$$

The electric field is then incremented by using the Poisson's equation:

$$E(x-\delta x) = E(x)- q*[Nd_{InGaAsSb} - n(x)]* [\delta x]/ \varepsilon_{InGaAsSb} \quad . \qquad (45)$$

The voltage in the elementary length δx is given by:

$$V(-\delta x) \quad = \quad [E(x)+ E(x-\delta x)]* [\delta x] /2. \qquad (46)$$

In order to proceed, the carrier density n(x) is incremented by using the following equation:

$$n(x-\delta x)=n(x)*\exp((-q*V(-\delta x)/(kb*T)) \quad . \qquad (47)$$

Poisson's equation is solved until the electric field becomes zero at x = -d1, which is the distance of the depletion region of interest. The differential voltages obtained are added to get a final voltage V. This voltage is compared with the assumed value of $\delta v1$. If both the voltages have the same magnitude and opposite sign then the chosen E0 is correct. The difference in the sign of $\delta v1$ and V is attributed to that the V is measured in reverse order compared to $\delta v1$. The chosen E0 is varied until both the voltages match.

Once the $\delta v1$ is matched by adjusting E0, then the calculations are carried out in the AlGaAsSb region, and Poisson's equation is used once again as :

$$dE/dx = \quad q * [Nd_{AlGaAsSb} - n(x)]/ \varepsilon_{AlGaAsSb}. \qquad (48)$$

The adjusted E0 is now used as the initial value for this equation. The initial value of carrier density is given by the following equation:

$$n(0) = nc1*\exp((q*(\delta v1 + \delta c1 - 0.75))/(kb*T)) \quad , \tag{49}$$

where nc1 is the carrier density in the conduction band of InGaAsSb. Poisson equation is solved in the same way as explained above. The electric field is incremented by using:

$$E(x+\delta x)=E(x)+([\delta x]*q*(nd2-n(x))/(\varepsilon_{AlGaAsSb}) . \tag{50}$$

The voltage in the elementary length δx is given by:

$$V(\delta x) = -[E(x)+ E(x+\delta x)]* [\delta x] /2. \tag{51}$$

The carrier density is then modified according to:

$$n(x+\delta x)=n(x)*\exp((q*V(\delta x)/(kb*T)). \tag{52}$$

Poisson's equation is solved until the distance x becomes x = l, where l is the given thickness of the AlGaAsSb region. The voltage V obtained is compared with the $\delta v2$ obtained from the equation:

$$-\delta e1-\delta v1+0.75 -\delta v2-E_{g2}- \delta e2 =Va. \tag{53}$$

If V matches $\delta v2$, then the chosen $\delta v1$ is deemed to be correct and E0 is the accurate electric field. If not, a different $\delta v1$ is chosen and the whole procedure is repeated until the all the values match.

CASE #2: When E0 is less than zero, the same above procedure is followed except that the $\delta v1$ is chosen to be positive. The above procedure can be explained by the following flowchart of Fig. 9.

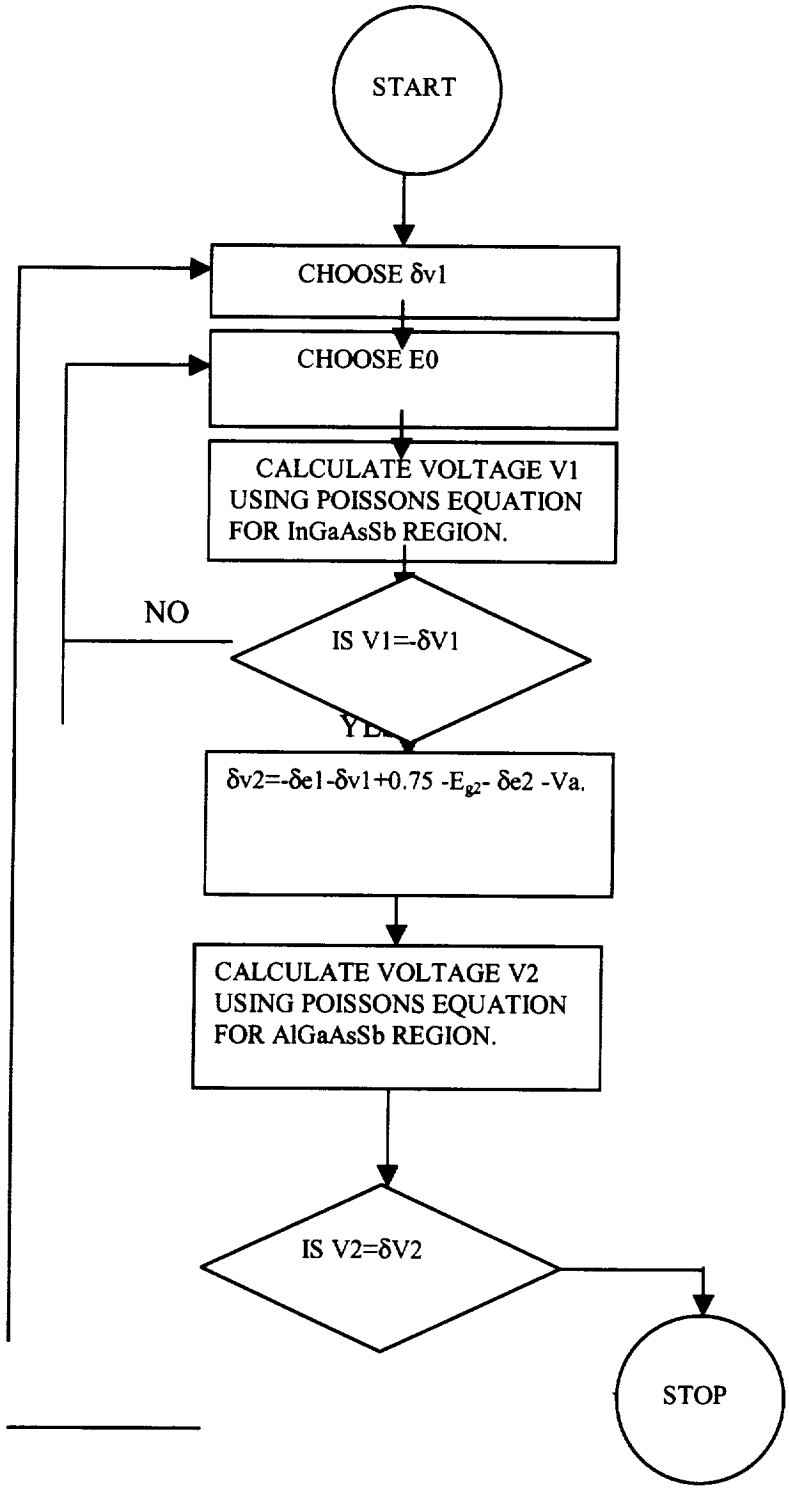

Fig. 9. Flow chart for calculating the electric field.

5.1 RESULTS AND DICUSSION

A.summary of the various results obtained in the analysis of the detector is provided in this section. The analysis has mainly been done to understand the electrical response characteristics of the existing structure, and to evaluate alternate structures. Calculating the current flow for the existing detector structure, on the basis of its energy band diagram, carries out the response analysis. This analysis also helps to find imperfections and shortcomings in the existing detector. Once such drawbacks are recognized, these can be overcome through the design of alternate geometries. It is shown that, unfortunately, the existing structure at NASA is lacking in these properties. Two alternate structures have been suggested, that should overcome the flaws inherent in the original detector design, and help achieve improved performance. These structures are obtained through various modifications of the original structure, which include varying the doping levels, and changing the thicknesses of detector sub-regions.

5.2 ENERGY BAND DIAGRAM OF THE EXISTING NASA DETECTORS

The energy band diagram for the existing detector can be obtained by combining the energy band diagrams of the three individual junctions of the detector. The junctions are n-GaSb:n-InGaAsSb, n-InGaAsSb:n-AlGaAsSb, and n-AlGaAsSb:p-AlGaAsSb. For convenience, these are referred to as the first, second and third junctions, respectively.

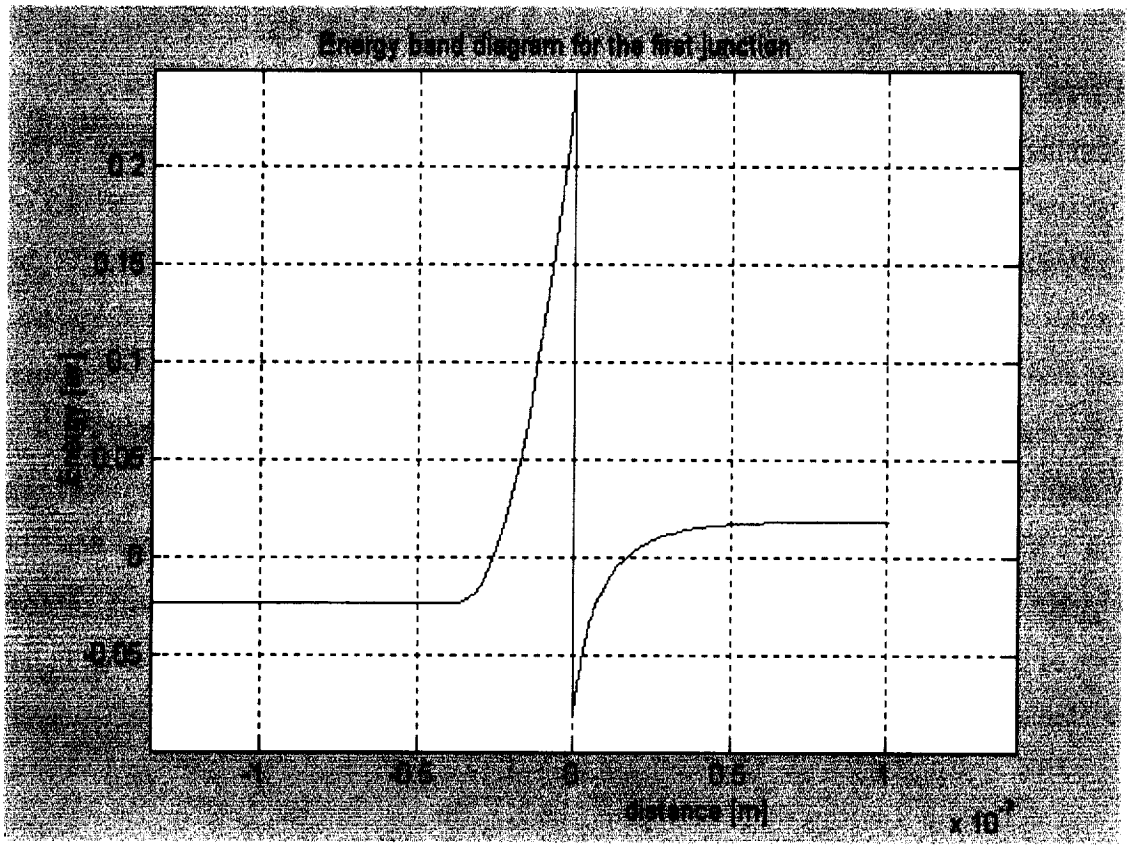

Fig. 10. The Energy band diagram of GaSb-InGaAsSb junction.

Figure 10 shows the partial energy band diagram (i.e. only the conduction band) for the n-GaSb:n-InGaAsSb junction. The valance band has been omitted for simplicity, since it lies E_g below the conduction band. The shape of the energy band diagram is typical of n-n heterojunctions [14, 15]. The energy variation is maximum at the origin (distance =0) and is equal to the band offset, which has a 0.325 eV value.

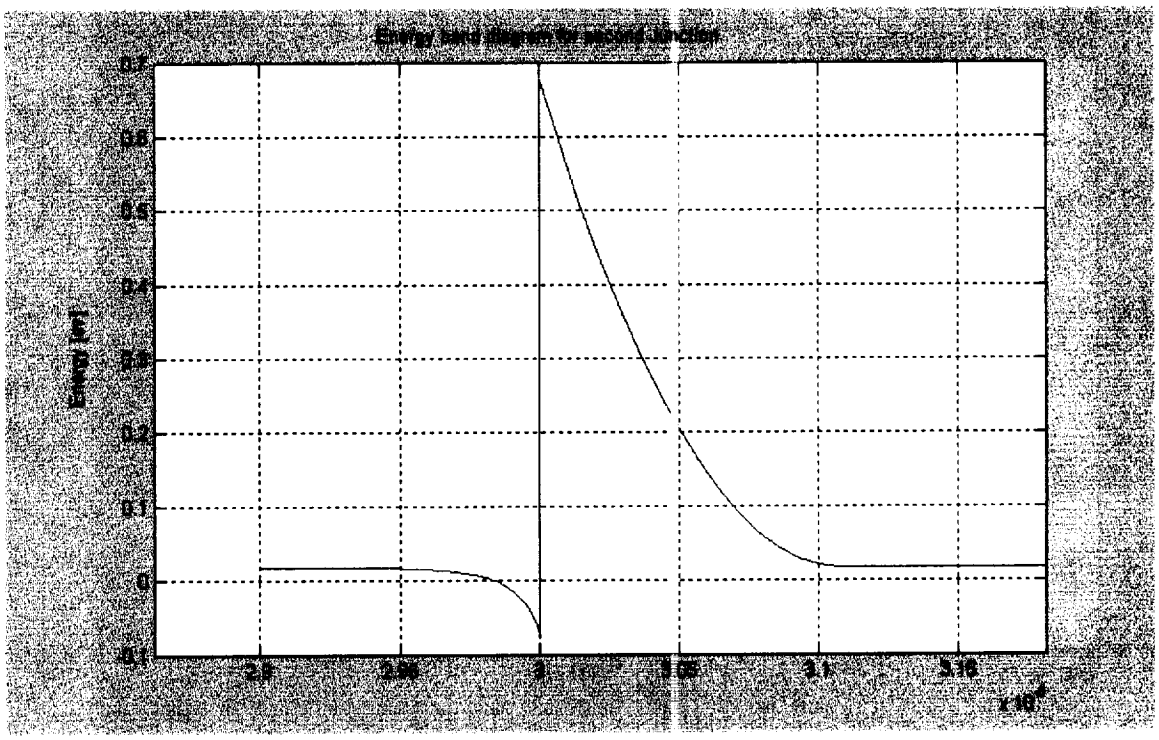

Fig. 11. The energy band diagram of InGaAsSb-AlGaAsSb junction.

The energy band diagram (conduction band) for the second junction is drawn in the same way as the first junction. Note that the origin of the second junction is at a distance d=3 μm from the origin of first junction (i.e. d = 0). This corresponds to the thickness [16] of the n-InGaAsSb region, which, for this detector is 3 μm.

The energy band diagram for the third junction resembles that of the conventional p-n junction. The origin of this diagram is at a distance d = 6 μm, since the AlGaAsSb [17] region in the NASA device is 3μm thick. Here, the energy band diagram penetrates more into the n-AlGaAsSb region as compared to the p-AlGaAsSb, because the p-AlGaAsSb region has a larger doping with respect to compared to n-AlGaAsSb region. Note that all the three energy band diagrams have been drawn with no external voltage applied i.e. when applied voltage is zero.

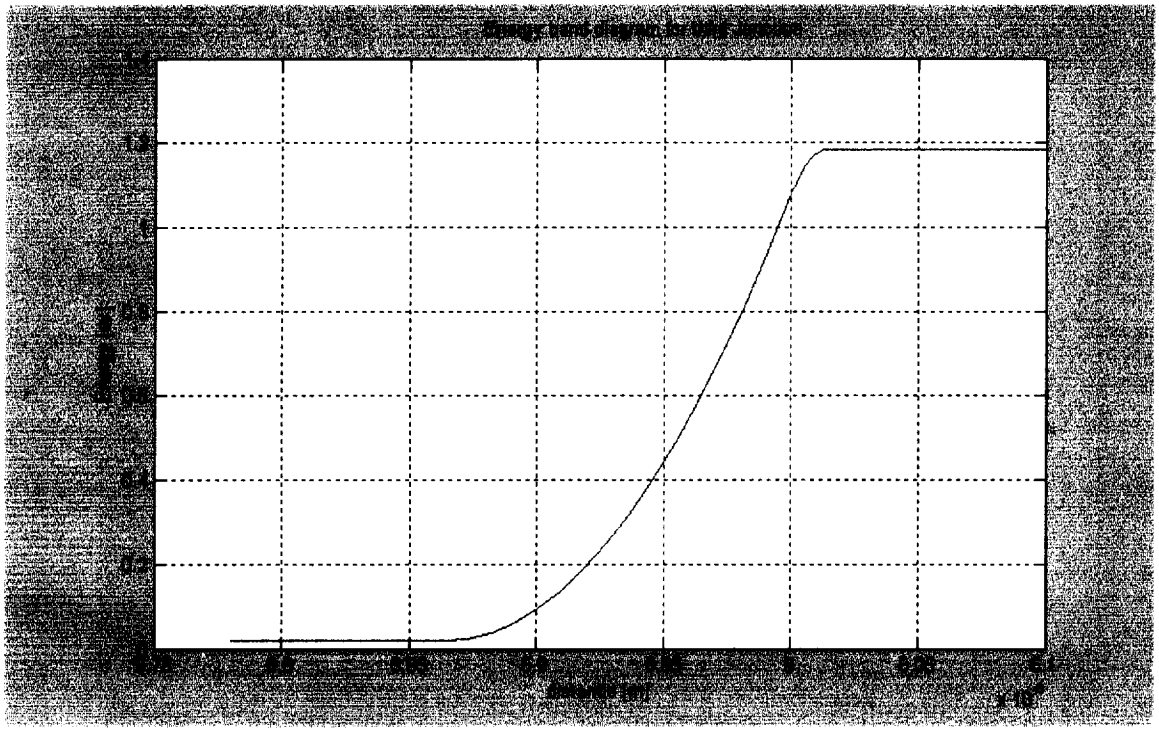

Fig. 12. The energy band diagram for AlGaAsSb p-n junction.

Once the energy band diagram for each junction has been obtained, the full energy band diagram can be deduced by combing each of the three individual segments. The combination has to be based on the condition that, when the current due to generation rate G_0 is neglected, the current flowing in each junction should be same for continuity. Consequently, the applied voltage will then divide between the junctions in such a way that the current at any point is the same and is equal to the total current flowing in the device. The idea similar to putting together a collection of resistors connected in series, subject to a constant total current, and a voltage division between the constituent resistive elements.

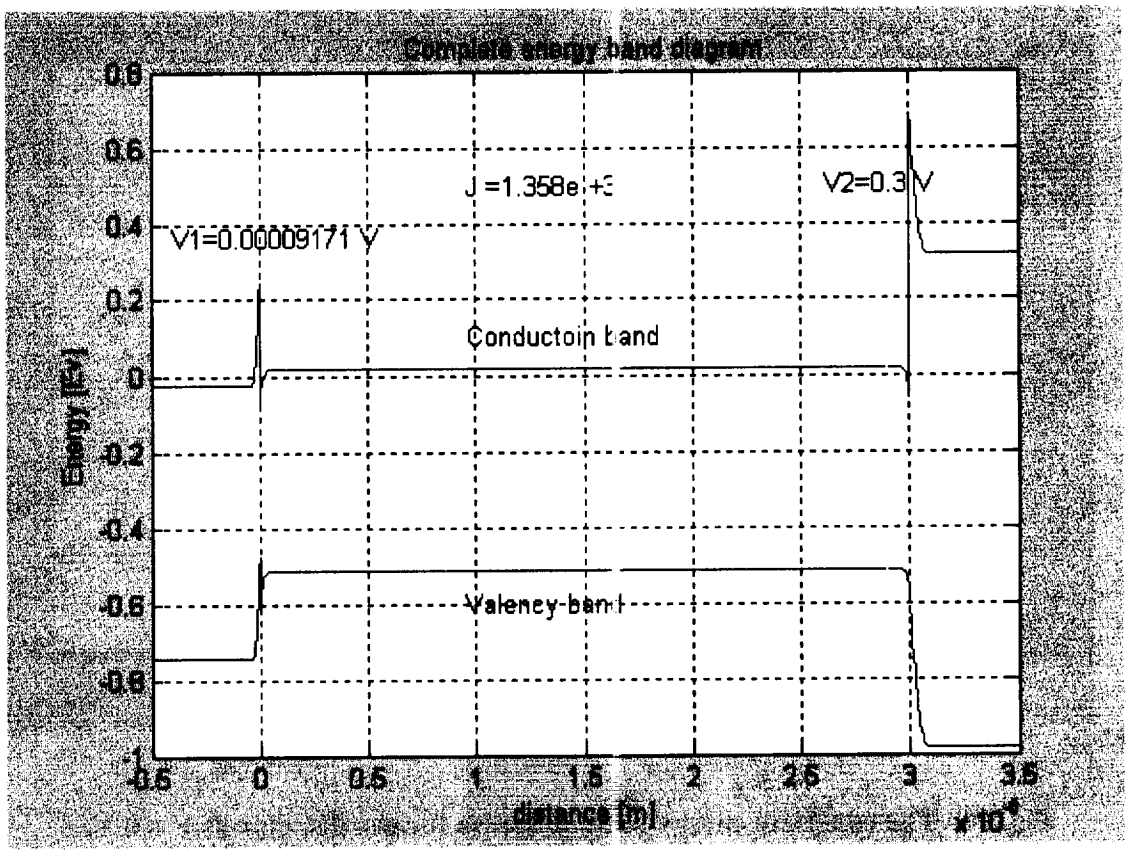

Fig. 13. The combined energy band diagram for the first two junctions.

Figure 13 shows the energy band diagram for the first two junctions based on the above voltage dividing principle. The voltage across the two junctions is divided in such a way that the total current is constant and is equal to $1.358 * 10^3$ A/m^2. This voltage division can be done from the J-V characteristics of the two junctions. From this, one obtains:

$$\text{Total applied voltage: } V = V_1 + V_2 = 0.30009171 \text{ V}, \tag{54}$$

$$\text{and, total current: } J \approx J_1 \approx J_2 \approx 1.358 * 10^3 \text{ A/m}^2. \tag{55}$$

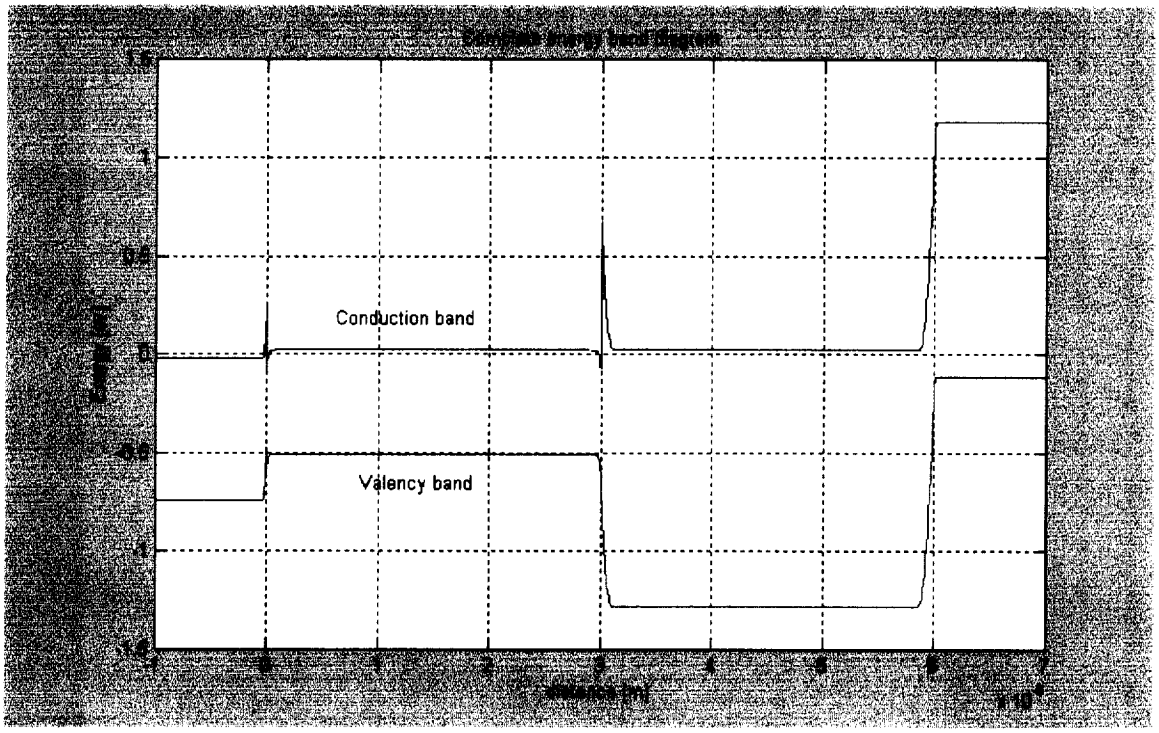

Fig. 14. The complete energy band diagram for the detector at V = 0 V.

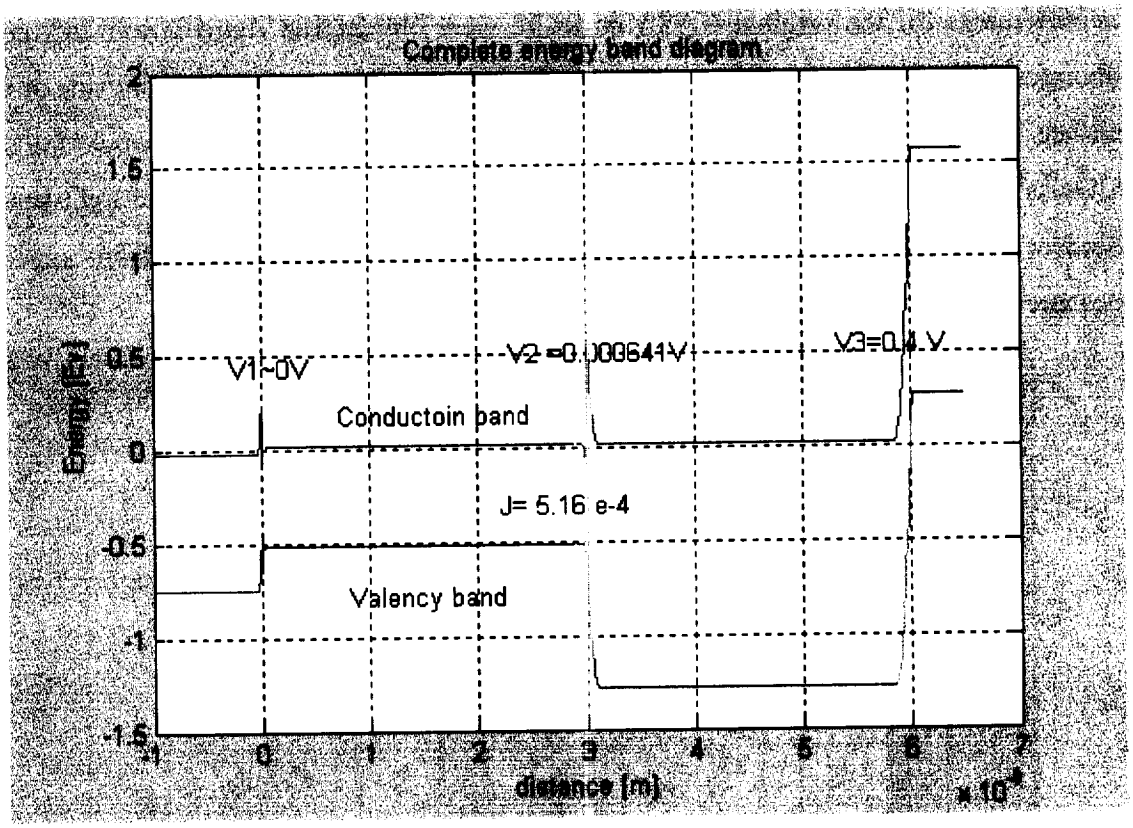

Fig. 15. The complete energy band diagram for the detector at V = 0.4 V.

Combining the energy band diagrams, as shown figure 14, draws the complete energy band diagram of the detector when no external voltage applied. The energy band diagram for the detector when an external, non-zero bias is applied is shown in figure 15. The applied voltage is equal to 0.400641 V. Most of the voltage is predicted to drop only across the third junction (V3 = 0.4V), to maintain a constant current equal to 5.16 x 10^{-4} A/m^2 in the detector. The negligible voltage drop in the first and second junctions can be explained on the basis of the J-V characteristics of the first and second junctions.

5.3 COMPARISION OF SIMULATION OUTPUT WITH NASA DATA

In this section, results of photodetector responsitivity for the existing NASA devices are compared with theoretical curves obtained from our simulations. The responsivity

measurements for the original NASA structure were obtained at Astro Power Inc. and other laboratories. Illumination on the detector could be incident from either the front side or the back surface. By convention, for front side illumination, light entering the detector would fall on the p-AlGaAsSb. Conversely, backside illuminated would be the situation for the light beam to be incident from the GaSb-side. The responsivity of the detector obtained from experimental measurements with front- and back-side illuminations, is shown in Fig. 16.

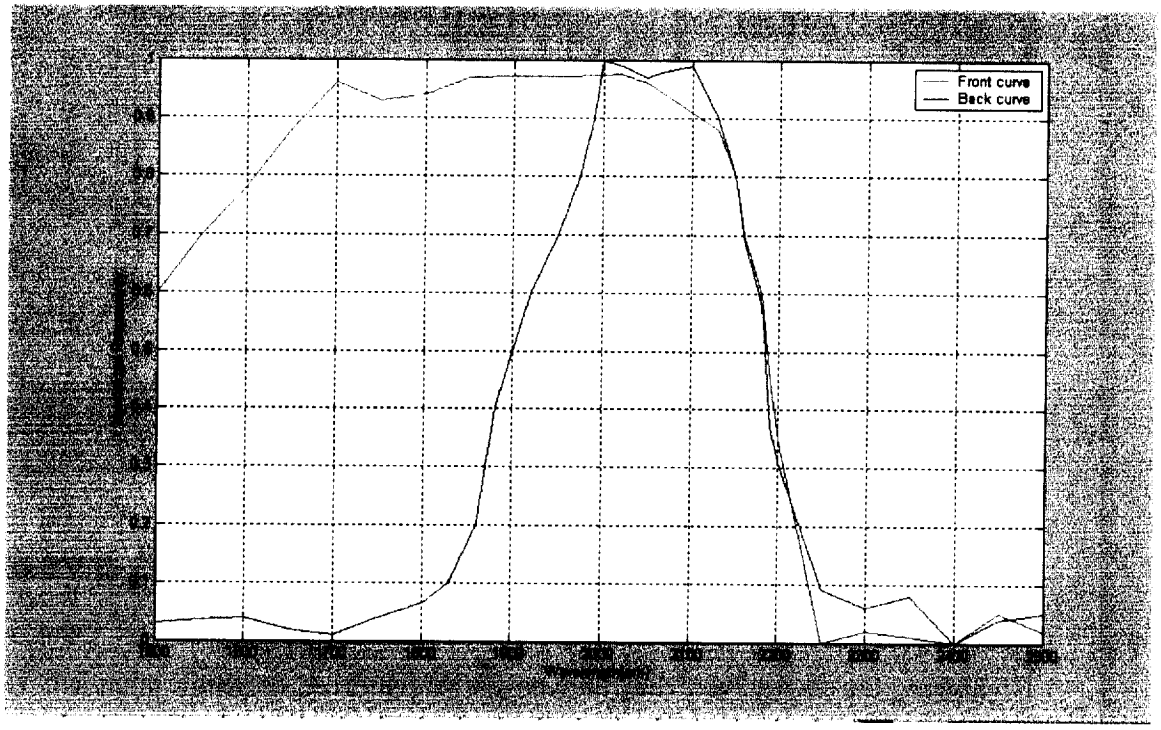

Fig. 16. Spectral response of front side and backside illuminated NASA structure [18].

As seen from the figure, the back-illumination curve has a maximum responsivity around the 2000 nanometers (nm) wavelength. The responsivity falls off quickly as the wavelength changes from 2000 nm. The "front" curve, on the other hand, has a responsivity that is constant from 2000-1700 nm, and then the responsivity begin to decrease slowly for lower wavelengths. The difference in their responsivities is due to the material that is primarily responsible of the photon absorption. For "backside" illumination, GaSb absorbs most of the light, particularly below the 2000 nm regime. This causes the resonsivity to fall sharply below 2000 nm in this mode of operation.

The absorption coefficient (α) of InGaAsSb for these curves is given to be 5.5 *10 ^{5} m^{-1} at 2000 nm. However, α is not a constant and changes with wavelength due to absorption by the band-edge "Urbach" tails, and increases in the density of states with energy. The variations of α were not measured, and neither are there any reports in the published literature. Given this unknown, the wavelength dependent alpha values were calculated from the responsivity of the "frontal-illumination" data curve. The alpha was assumed to be nearly constant in the region below 2000 nm. The resulting alpha variation thus obtained from the responsivity measurements, is shown in Fig. 17.

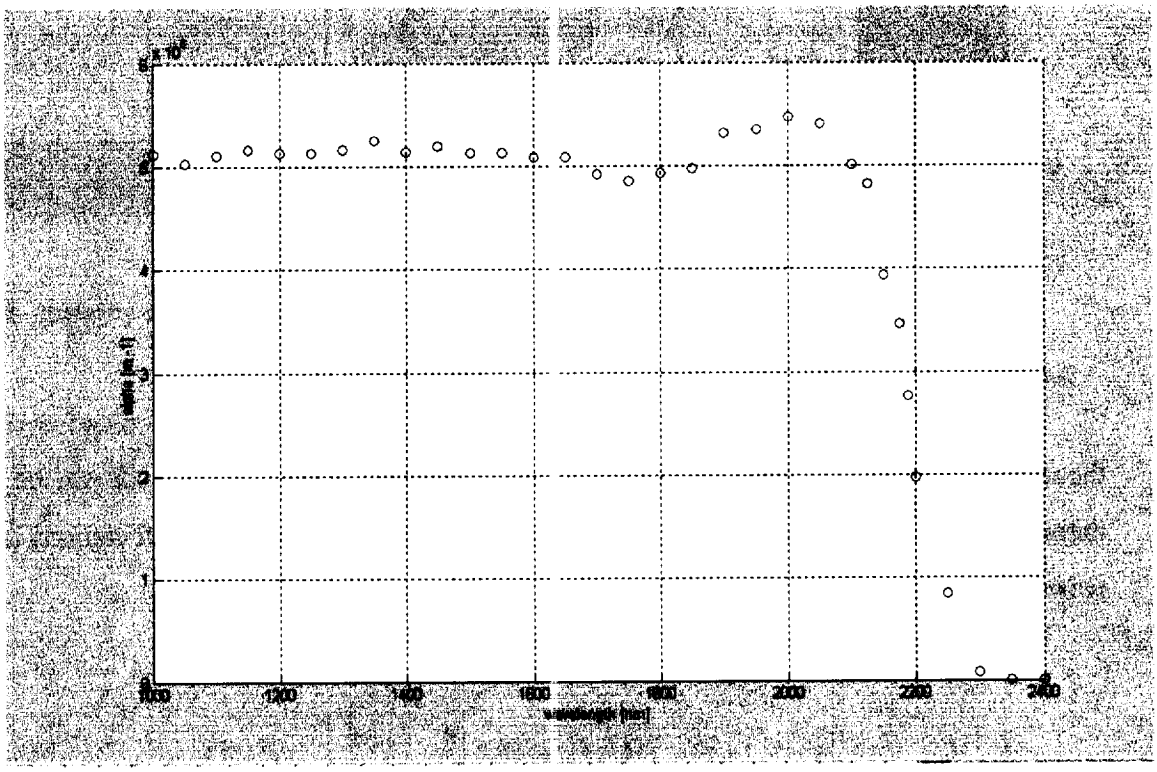

Fig. 17. Alpha versus wavelength for the existing NASA detector.

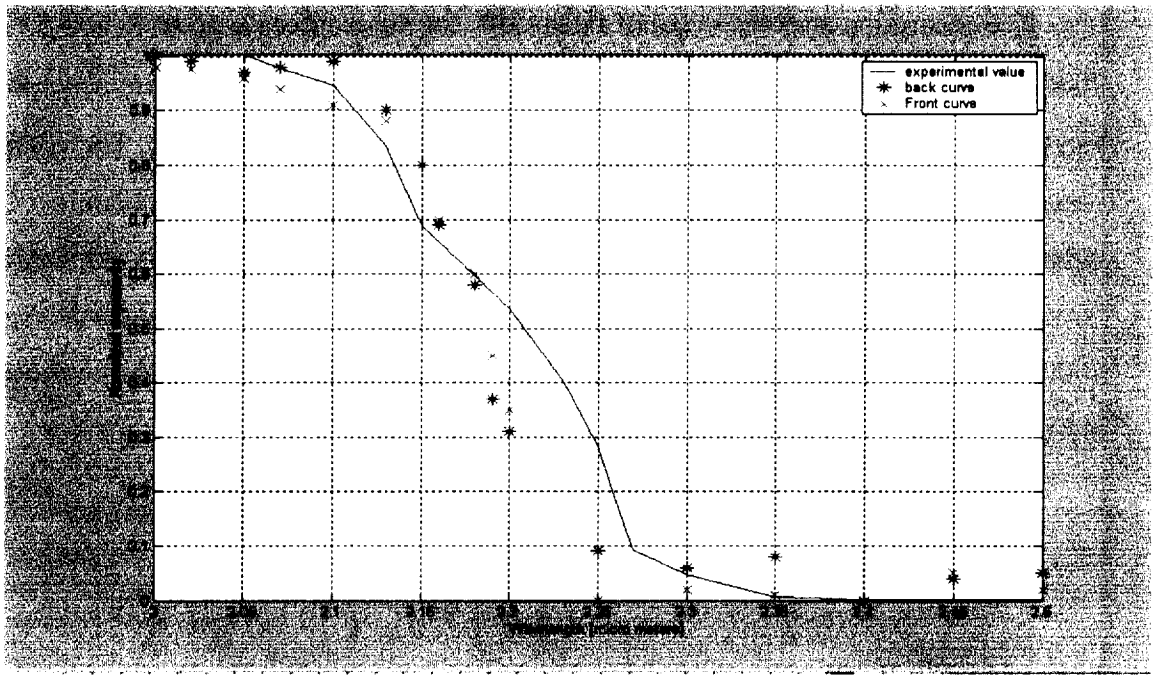

Fig. 18. Comparison of experimental responsivity with the existing data.

Shown in Fig. 18 are the experimental data for the normalized responsivity, and a theoretical calculation based on the calculated alpha curve of Fig. 17. As can be seen, the theoretical predictions match both the front and back curves fairly well. Deviations at the long wavelengths are probably due to device leakage currents.

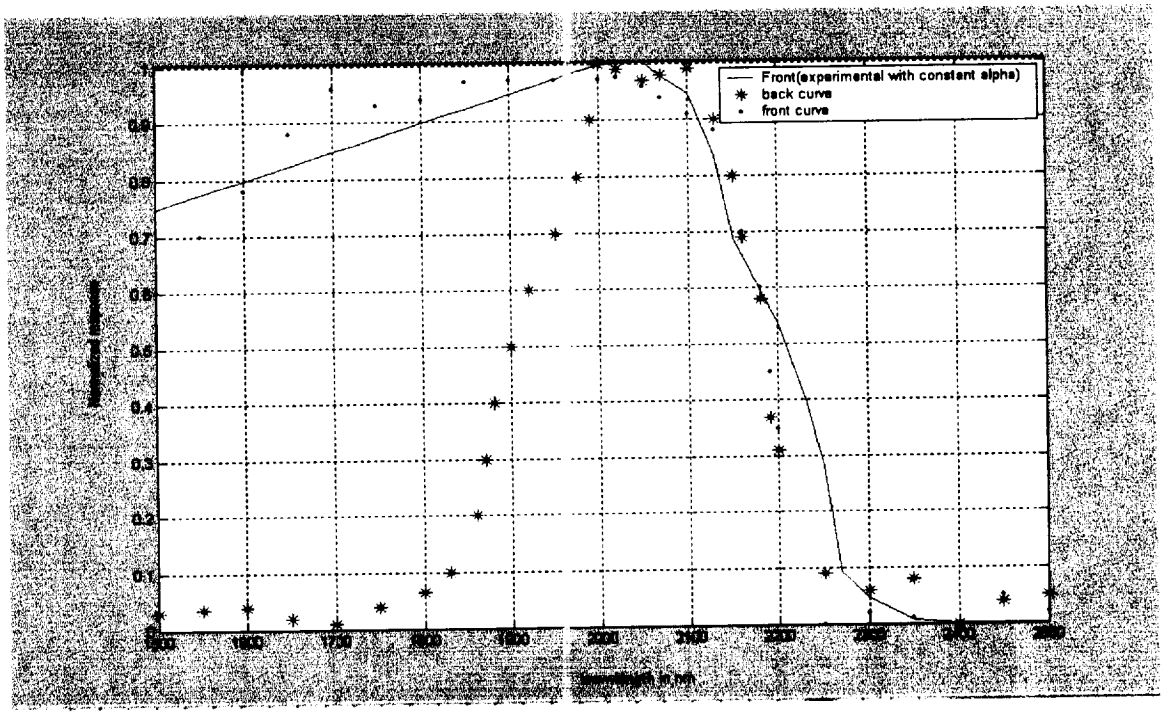

Fig. 19. Comparison of experimental and NASA curves for front illumination.

For alpha assumed to be nearly constant for wavelengths below 2000 nm, the theoretical responsivity obtained is shown in Fig. 19. The experimental data roughly matches the calculated curve. The experimental curve is also drawn for the backside illumination case, for completeness. As seen from the figure, the experimental curves are nearly identical for both the front- and back-side illumination situations for wavelengths greater than 2000 nm, while they differ for lower wavelengths. This difference is arises because upon backside illumination of the device, the absorption from the GaSb layer causes an additional decrease in photon intensity. This causes the responsivity to fall more quickly. The experimental back curve has the same shape as the theoretical curve, but falls more rapidly after 1800 nm wavelengths.

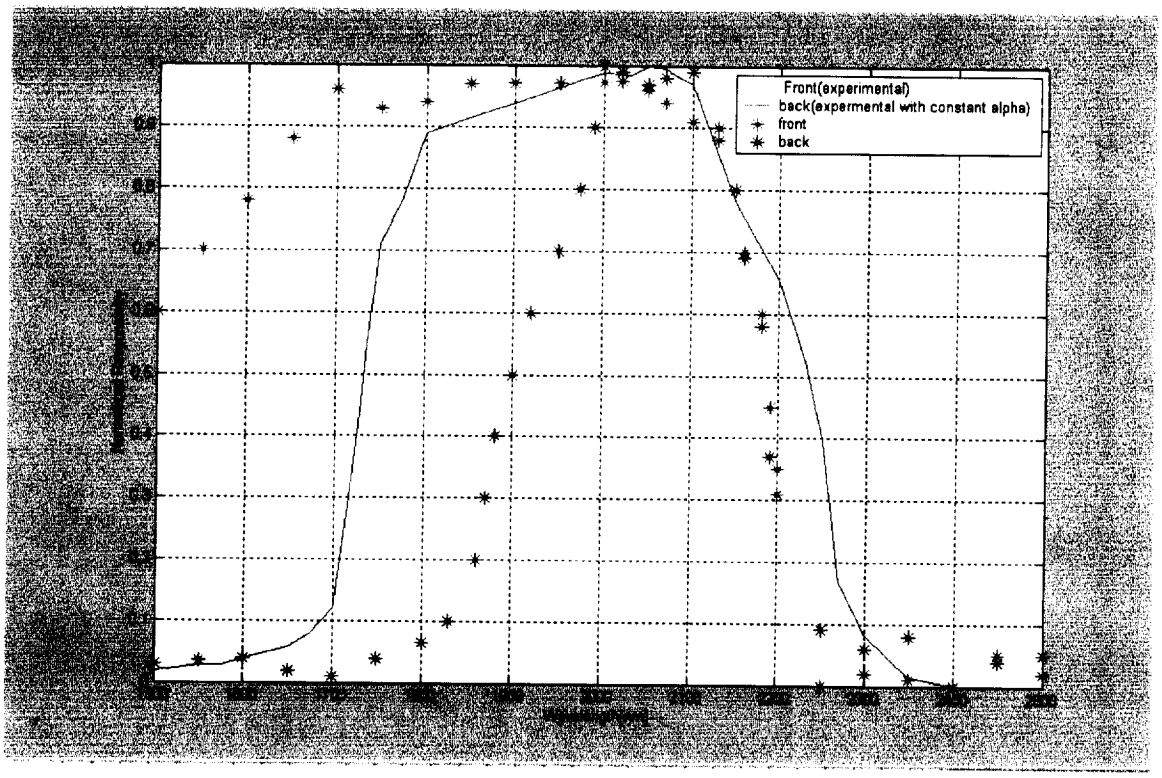

Fig. 20. Comparison between experimental data and theoretical curves.

The other structures available and tested at NASA were also studied, and their responsivity values compared. For example, wavelength-dependent responsivity for NASA structure D19-K204-11#8 , had a response as shown in Fig. 21.

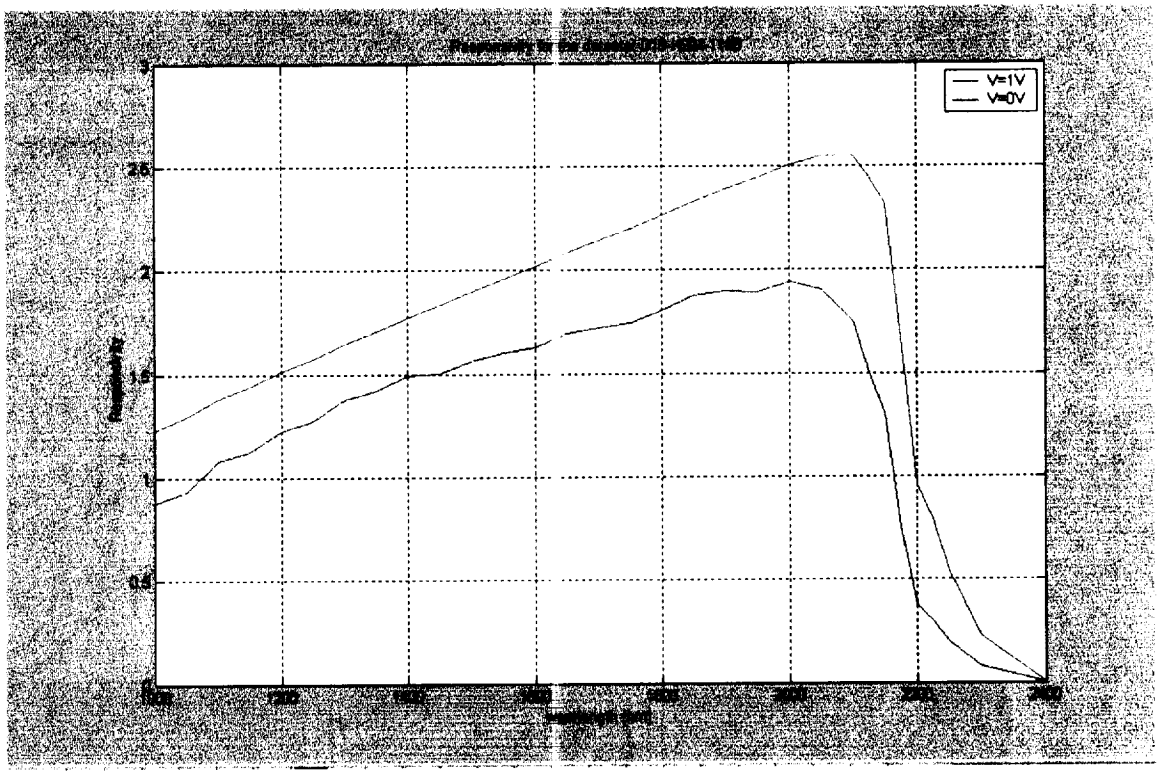

Fig. 21. Responsivity versus wavelength for D19-K204-11#8 detector.

The responsivity versus wavelength curves for the NASA detector **D19-K204-11#8** at the two applied voltages of 0V and 1V, are shown in figure 21. As seen from the plots, an increase in voltage causes a corresponding increase in the responsivity for a given wavelength. These experimental data are compared with the theoretical predictions obtained from the extracted alpha values of figure 17. The resulting plots are shown in figure 22. As seen from figure 22, the experimental data and calculated responsivity match almost exactly for V = 0V, and also are in nearly agreement at the 1V bias. This validates the alpha values and bears out the theoretical modeling.

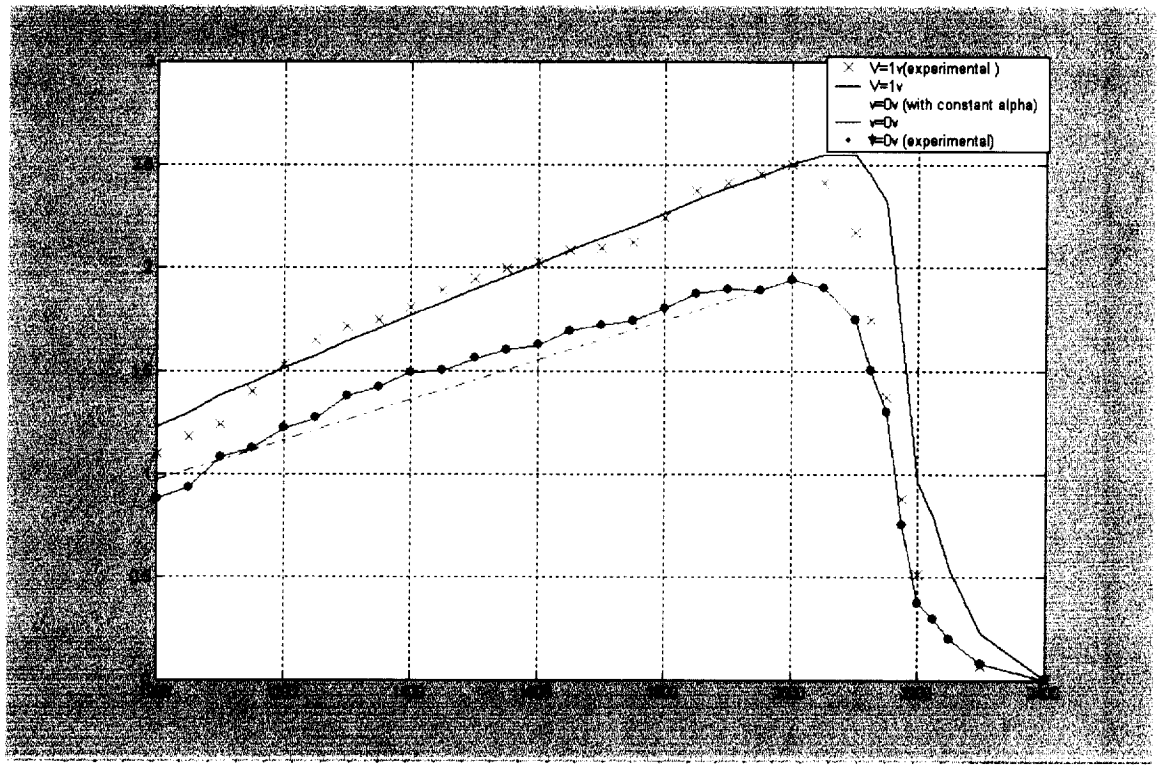

Fig. 22. Comparison between experimental and existing curves for D19-K204-11#8.

5.4 ANALYSIS OF EXISTING DETECTOR STRUCTURE

The characteristics, including the energy band diagram, for the photo-detector existing at NASA LaRC have been explained in the previous section. The detector was designed for several NASA applications mainly at the 2μm wavelength. In order to enhance the sensitivity, it is highly desirable to achieve internal carrier multiplication and avalanche action for amplifying the photo-current. Unfortunately, the current detector described in the previous section seems to have several flaws in its design. First, the dark current of the detector, which should ideally be small for low background noise detection, is actually large. The dark current in this detector is in the same orders of magnitude as the photo current. This makes it very difficult to distinguish between the actual photocurrent response, and the dark currents. The detector also suffers from the problem of being able to achieve high carrier multiplication. The avalanching property is useful because, in most of the

detectors, the incoming signal will be weak. This is especially so if the incoming photon signal is weak due to atmospheric attenuation. For good detection, such as weak signal needs to be amplified to produce a strong, distinguishable output. Therefore, without avalanche action and internal gain through carrier multiplication, it is very difficult to detect weak signals. This is, therefore, is one very important drawback of this detector that needs to be corrected. The following section present alternate structures that attempt to rectify the above flaws.

5.4.1 GUIDING PRINCIPLES FOR GOOD PHOTO-DETECTION

The following steps should be taken for improving the performance of the photo-detector. The main aim is to reduce dark current and increase the photo-current.

1. Reduce the doping N_d within the n-InGaAsSb region. The reduction of doping N_d will increase the width of depletion layer in that region. This would also cause a decrease in the carrier recombination, since relatively fewer free carriers would be available for direct recombination. The reduction in carriers also brings about a reduction in the dark current. This would effectively work to suppress the background noise. This is the main advantage of reducing the doping in InGaAsSb region. Reducing doping also increases the resistance in that region which will increase the IR voltage drop. Consequently, the electric field would increase. This in turn, can facilitate an increase of the drift current, and the possibility for carrier impact ionization.
2. Reductions in doping within the n-AlGaAsSb region, and to make it nearly intrinsic, if possible. This reduction in doping would help in reducing δEv [22] between the InGaAsSb-AlGaAsSb regions by pushing up the AlGaAsSb energy band diagram. This will also help increasing the electric field necessary to drive the holes and to cause impact ionization in the p-n junction. Finally, the possibility of tunneling in p-n junction can also be avoided by reducing the doping.
3. Reducing the width of AlGaAsSb region. This reduction will cause the electric field in the n-p junction to penetrate deeper into the InGaAsSb region. This also reduces possible

recombination. Finally, the reduced width will lower the carrier transit time, thereby, increasing the frequency response and speed.

5.5 ANALYSIS OF TWO ALTERNATE DEVICE STRUCTURES

In keeping with the above strategies, two alternate photo-detector structures are proposed for improving the performance of the existing device. In both the alternate structures, the n-GaSb region is completely removed, as it really does not serve any useful role in either the carrier absorption, or multiplication processes. The two alternate structures are:

1. An intrinsic InGaAsSb-Intrinsic AlGaAsSb- p AlGaAsSb detector, and
2. An intrinsic InGaAsSb-p (lightly doped and almost intrinsic) AlGaAsSb-p AlGaAsSb detector.

The analysis of the above two structures is done, in an attempt, to see if the performance can be improved. The first structure consists of very lightly n-InGaAsSb (almost intrinsic) with a doping concentration of 10^{22} m^{-2}, and n-AlGaAsSb (almost intrinsic) with a doping concentration of 5×10^{21} m^{-2}, and a p-type AlGaAsSb region. Note that the width of the AlGaAsSb region is reduced to 1 μm from the 3 μm dimension of the original detector.

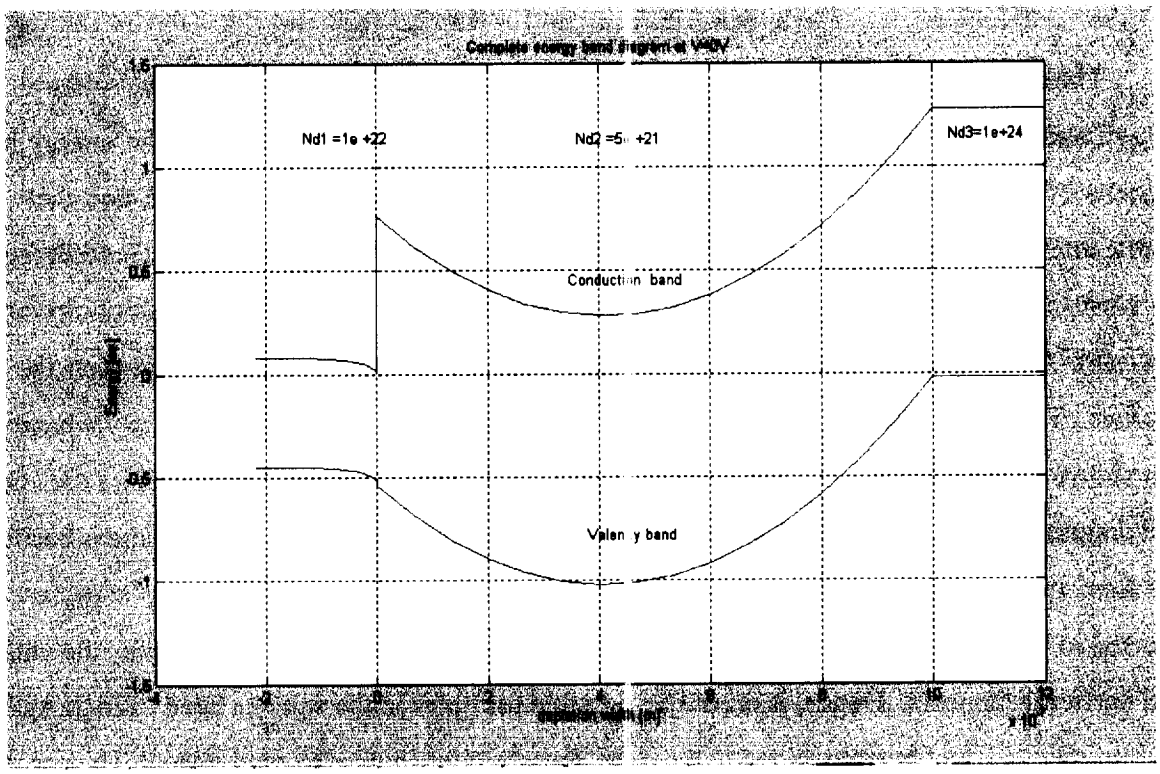

Fig. 23. The complete energy band diagram of the modified structure1 at V = 0V.

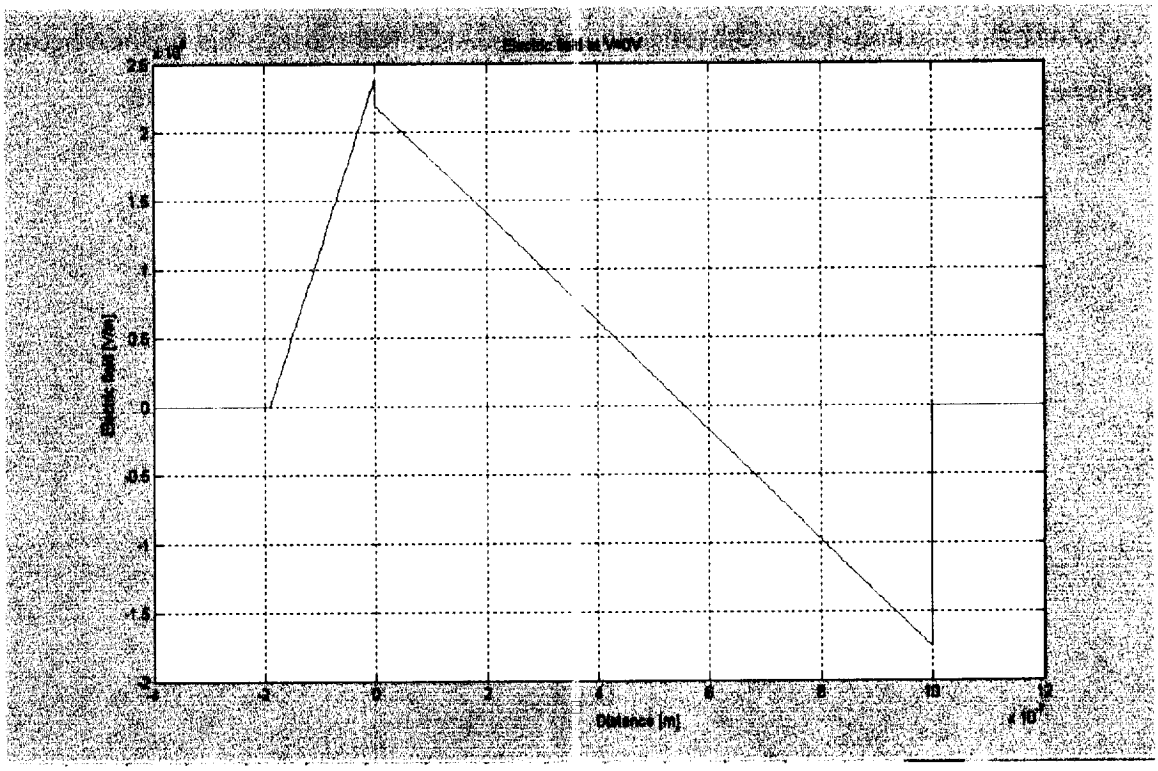

Fig. 24. The electric field for the modified structure1 at V = 0V.

The energy band diagrams of the above structures were calculated at different voltages. The energy band diagram with no applied voltage is shown in figure 23. Note that the energy band diagrams of n-InGaAsSb-n-AlGaAsSb and AlGaAsSb p-n junction are combined, and there is a definite inter-penetration of electric field from the AlGaAsSb p-n junction into the InGaAsSb region. The corresponding internal electric field profile is shown in Fig. 24. The discontinuity at the InGaAsSb-AsGaAsSb junction is due to the difference in dielectric constants between the two materials. The energy band diagrams for other applied voltages ranging from 0.5 V to 7V have also been shown in Figs. 25-29. As seen from the figures, the increase in the voltage causes the energy band diagram to shift up in InGaAsSb-AlGaAsSb region. For voltages below 2 V, there is barrier to hole flow in the n-AslGaAsSb region. Hence, the photocurrents at such biasing levels are not expected to be very large. However, as the biasing voltage reaches beyond a 2V value, the valance band barrier disappears. Hence, it should be possible for holes in the valance band of InGaAsSb to move unimpeded, and be transported to the right, thereby contributing to a net current. The very high electric field will promote high drift velocities, and could even cause impact ionization at the AlGaAsSb p-n junction. The width reduction of AlGaAsSb will enhance this, not only because of the higher electric fields, but also of negligible recombination over a narrower width.

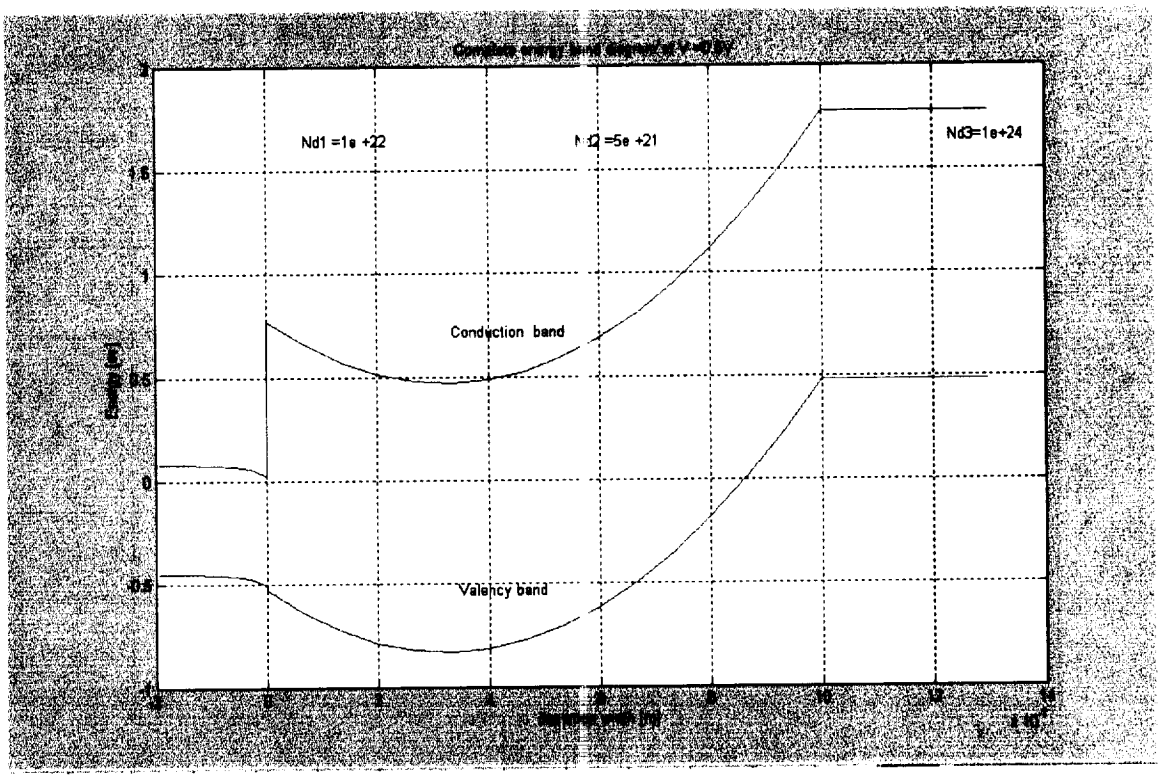

Fig. 25. Complete energy band diagram of the modified structure1 at V = 0.5V.

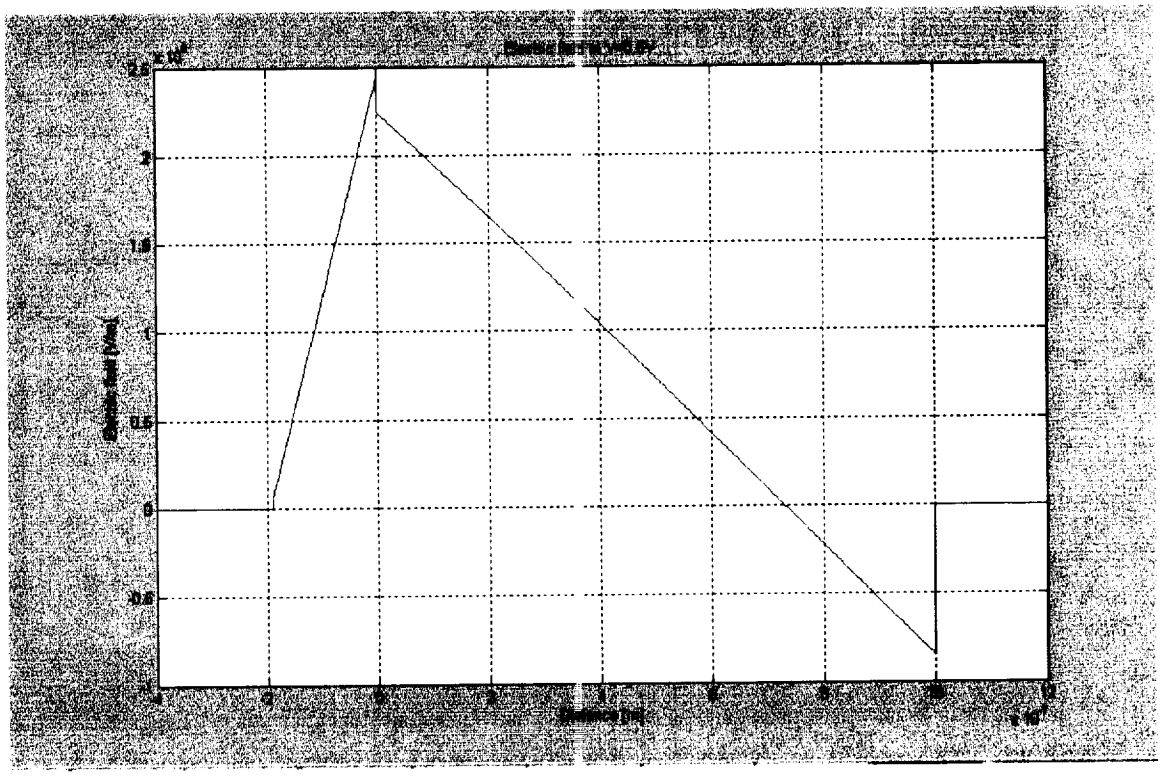

Fig. 26. The electric field for the modified structure1 at V = 0.5V.

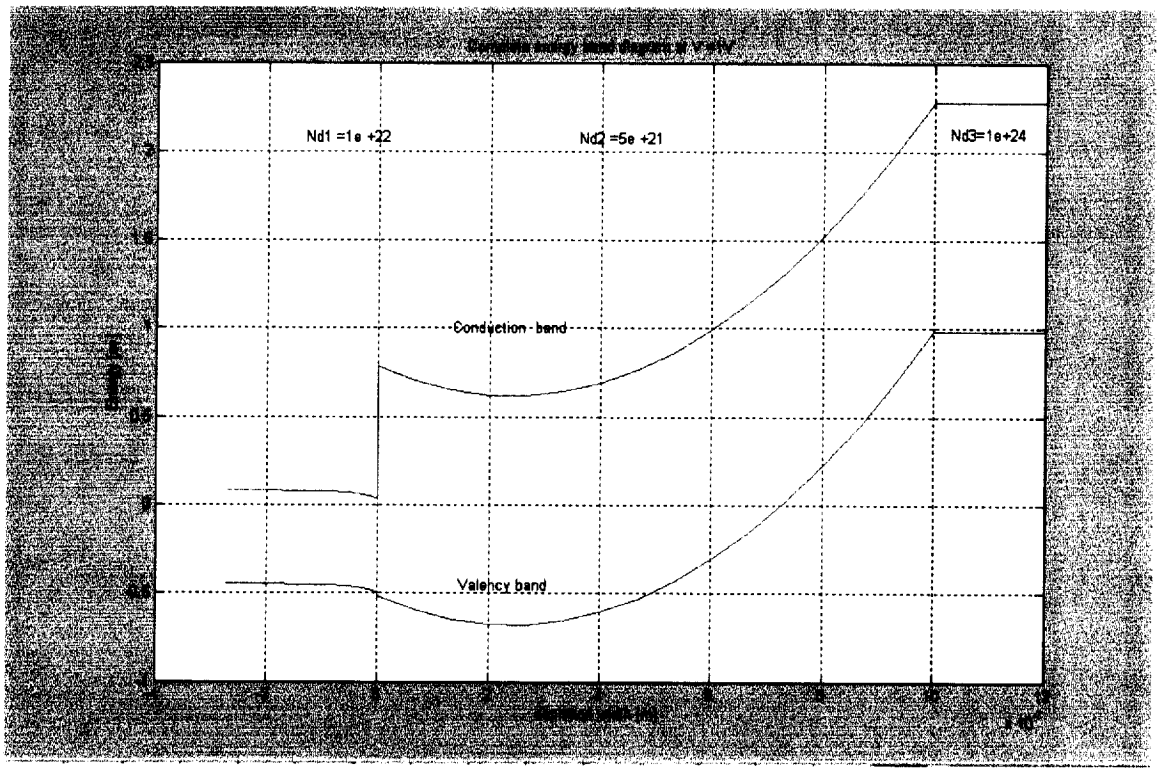

Fig. 27. Complete energy band diagram of the modified structure1 at V = 1V.

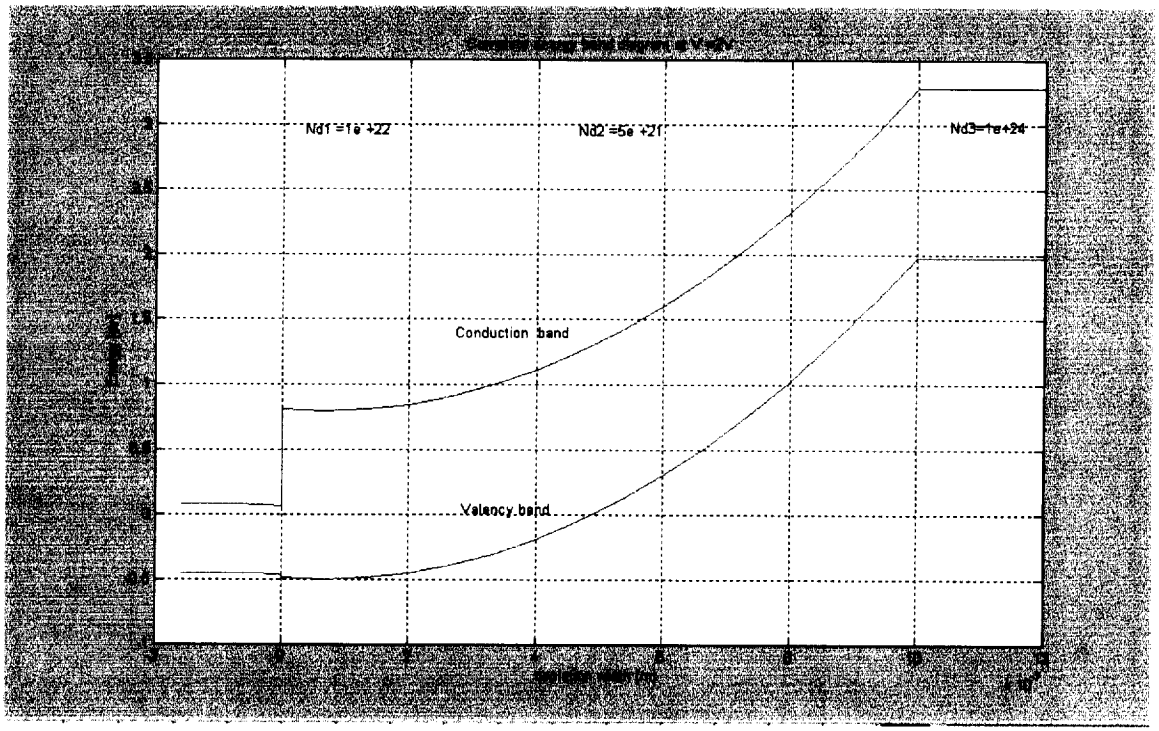

Fig. 28. The complete energy band diagram of the modified structure1 at V = 2V.

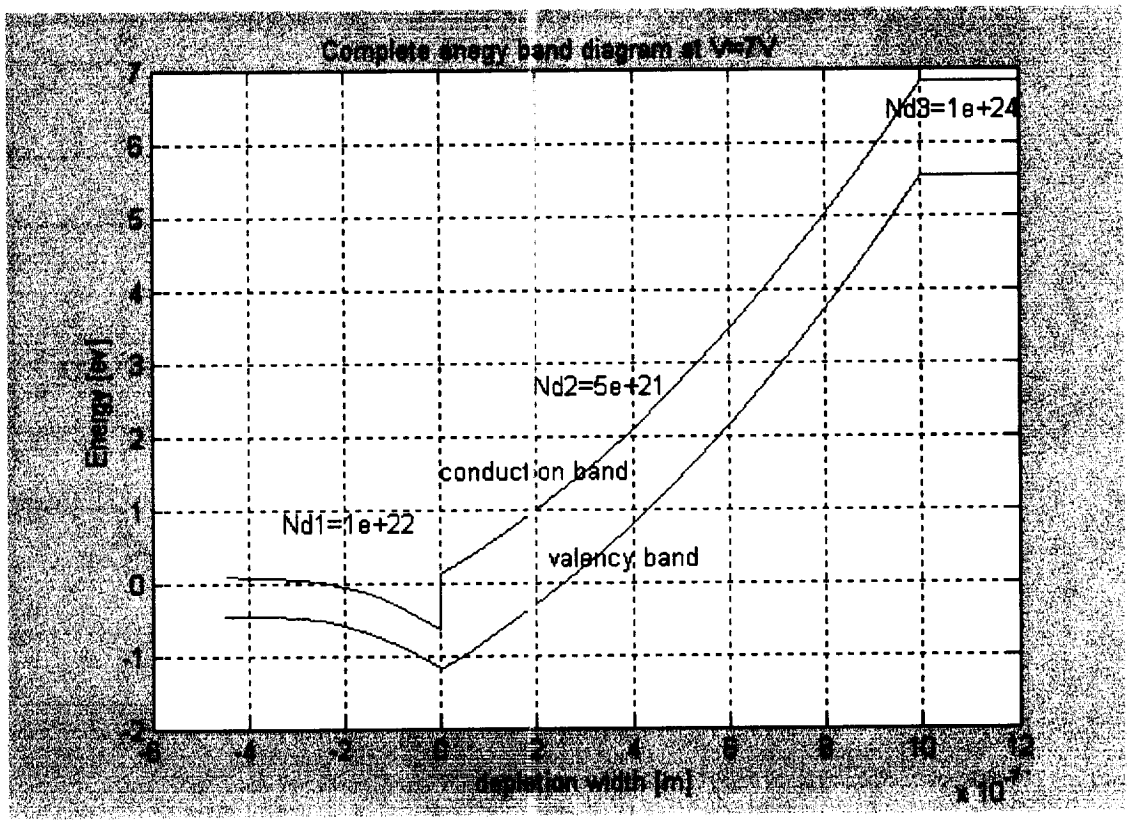

Fig. 29. Complete energy band diagram of the modified structure1 at V = 7V.

The above structure is also predicted to have a low dark current because of reducing doping. This bodes well for the overall selectivity and detectivity of the device. Also, a large photocurrent should result, given the possibility for carrier avalanche at high biasing, and low recombination along the transit path. The large band bending is indicative of the potential for high impact ionization.

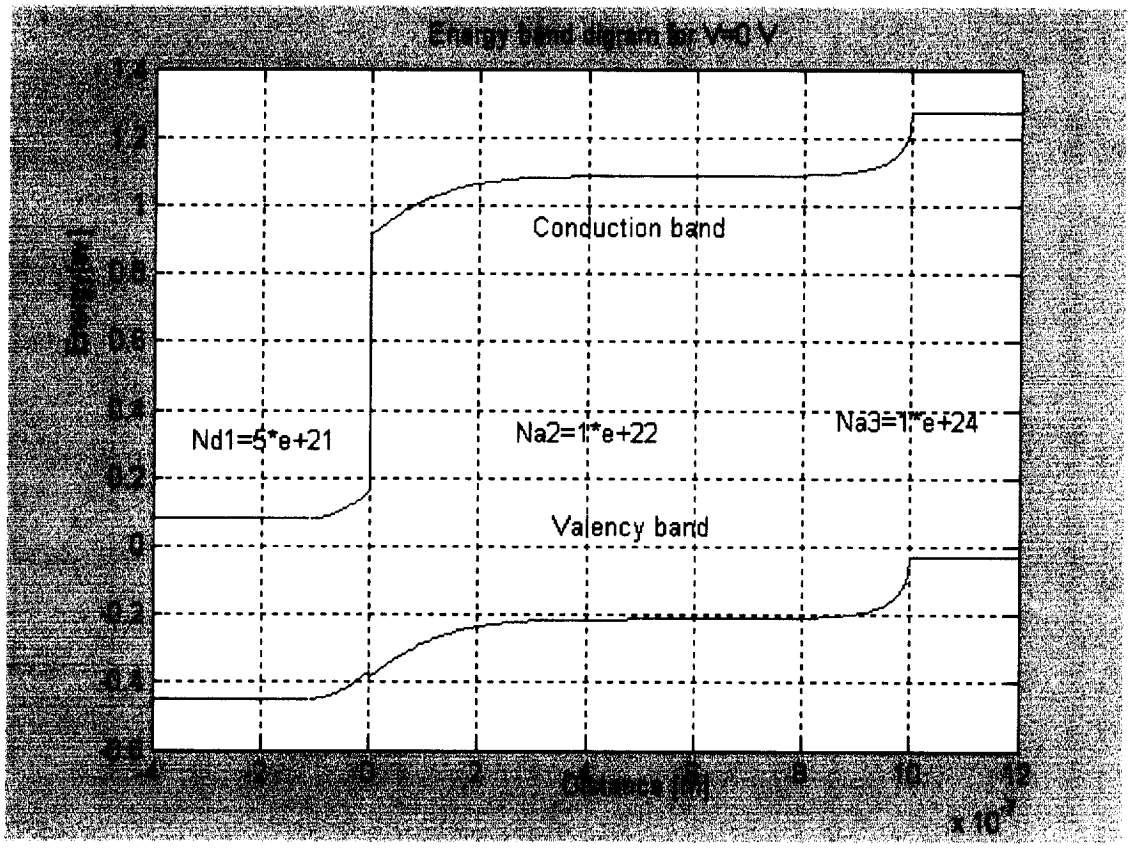

Fig. 30. The complete energy band diagram of the modified structure2 at V = 0V.

A second structure is now proposed and investigated. The second structure consists of very lightly n-InGaAsSb (almost intrinsic) with a doping concentration of 10^{22} m^{-3}, and p-AlGaAsSb (almost intrinsic) with a doping concentration of 5 x 10^{21} m^{-3}, and a p-type AlGaAsSb region. Note that, similar to the first structure, the width of the AlGaAsSb region is maintained at 1μm. The energy band diagrams for the second structure were also calculated, and the shown for various applied voltages in the following diagrams. Fig. 30 is for a zero bias case, the diagram of Fig. 31 for 0.5 V and Fig. 32 for 2 V bias.

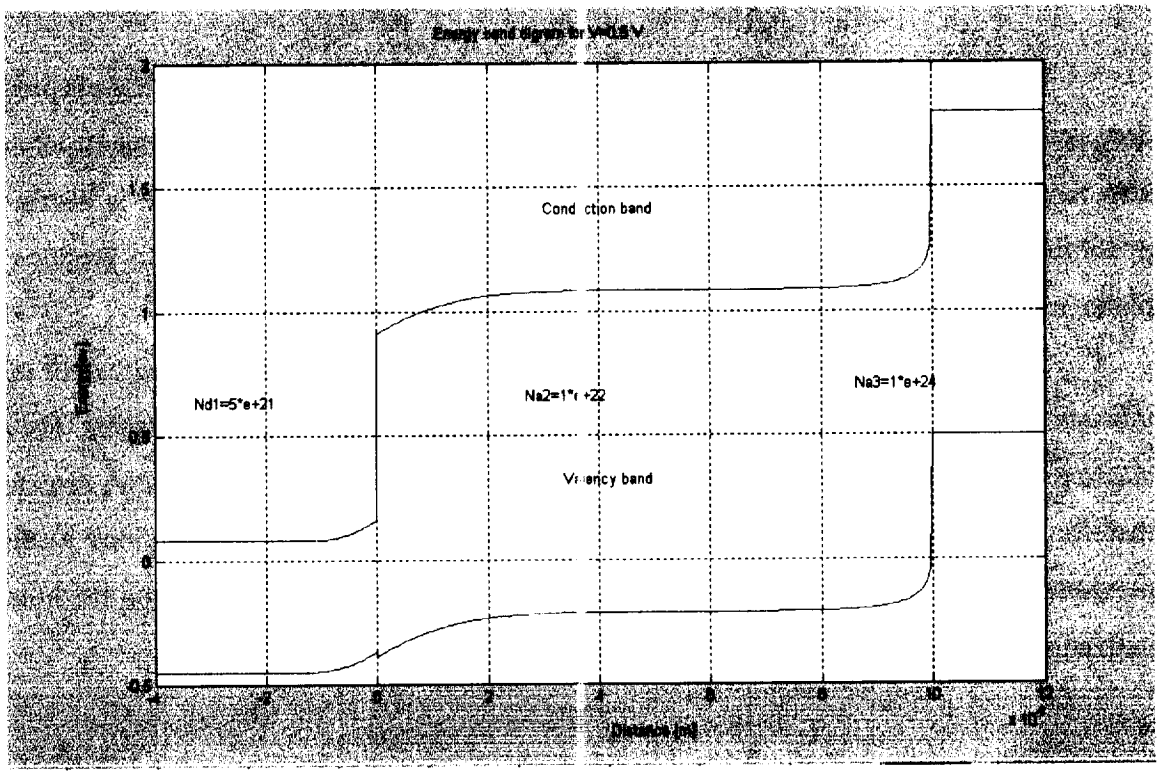

Fig. 31. Complete energy band diagram of the modified structure2 at V = 0.5V.

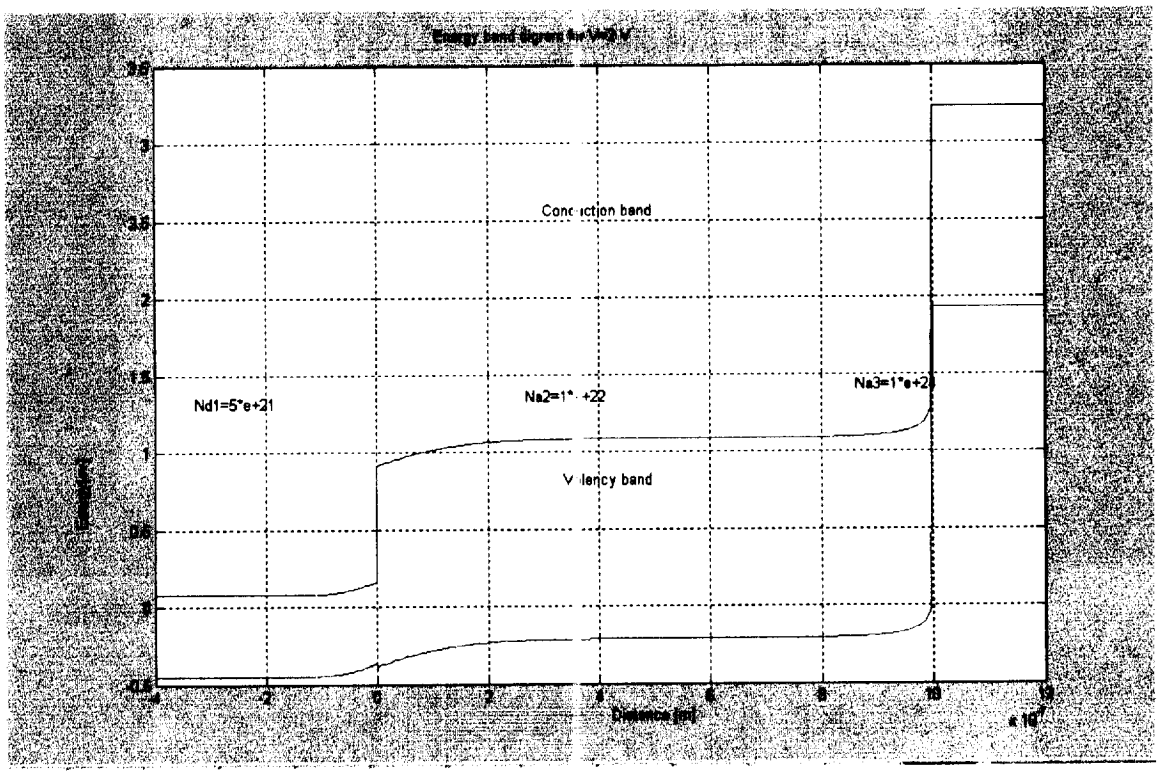

Fig. 32. The complete energy band diagram of the modified structure2 at V = 2V.

In this second structure, as the applied voltage increases, most of the voltage is predicted to drop across the AlGaAsSb p-n junction. Like the first structure, this device scheme structure would also help drift holes in the InGaAsSb and AlGaAsSb valance bands. There is also a distinct possibility to cause impact ionization across the AlGaAsSb junction, and to produce a large photocurrent.

Since the success of these photo-detectors depends on the degree and extent of impact ionization for internal gain, it is necessary and germane to evaluate the ionization rates. The hole and electron impact ionization rates for the AlGaAsSb region of the existing NASA detector were, therefore, calculated for different applied electric fields and for different compositions. As discussied previously and shown in Fig. 6, the change in the composition, has no effect on the hole impact ionization coefficient (β) [23-25]. However, the electron

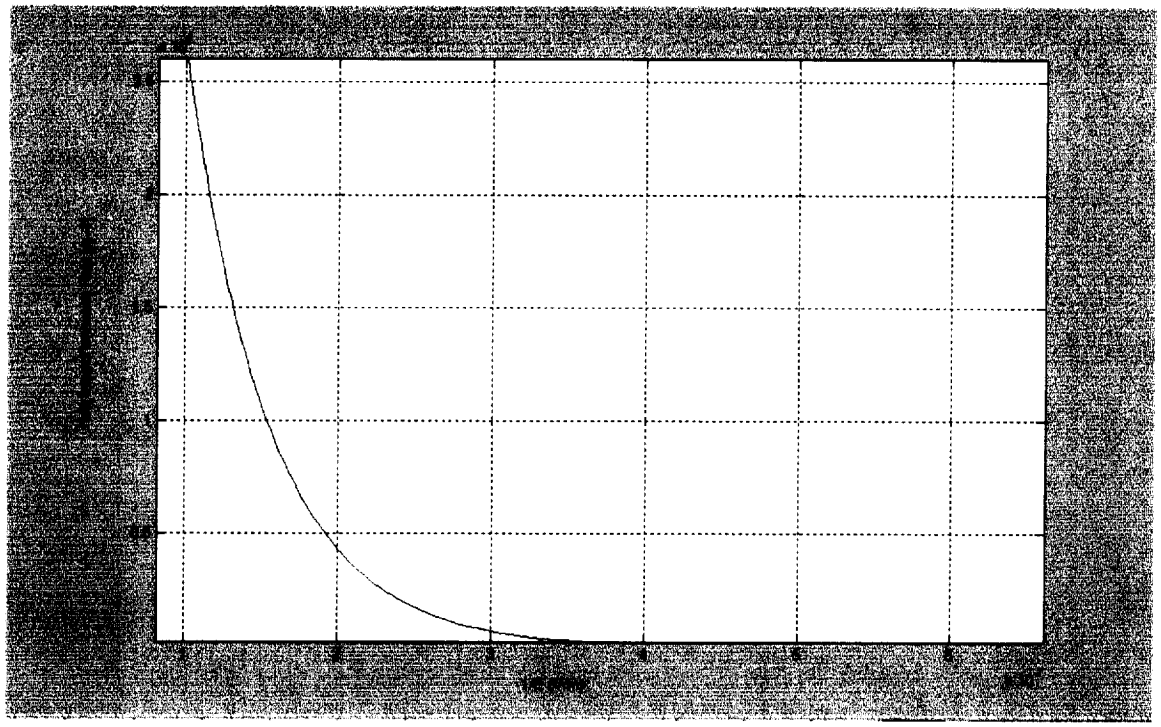

Fig. 33. The hole impact ionization rate versus inverse of electric field.

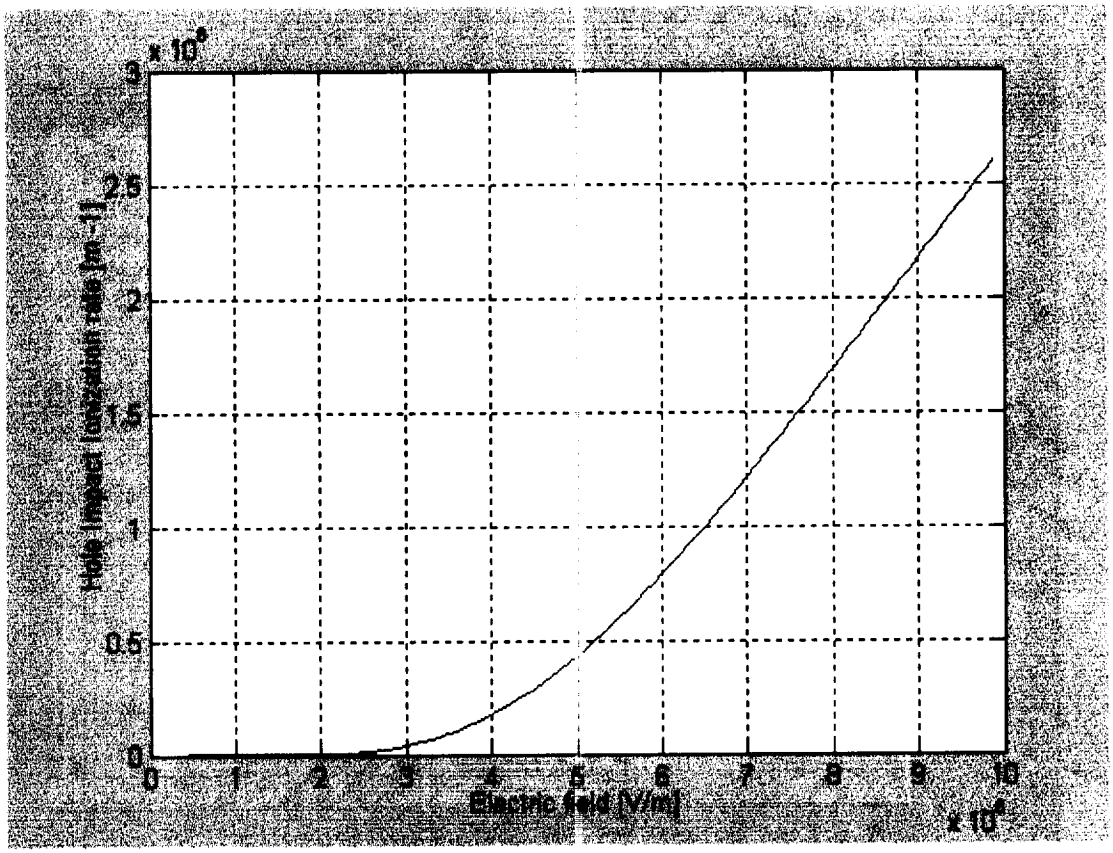

Fig. 34. The hole impact ionization rate versus electric field.

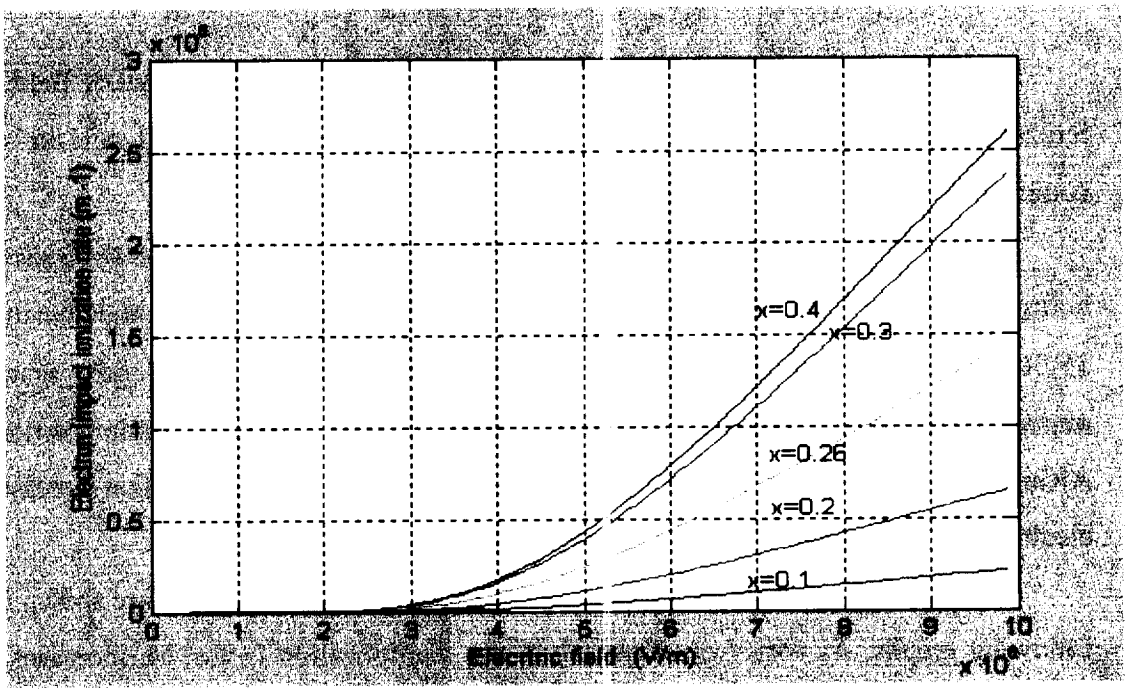

Fig. 35. The electron impact ionization rate versus electric field.

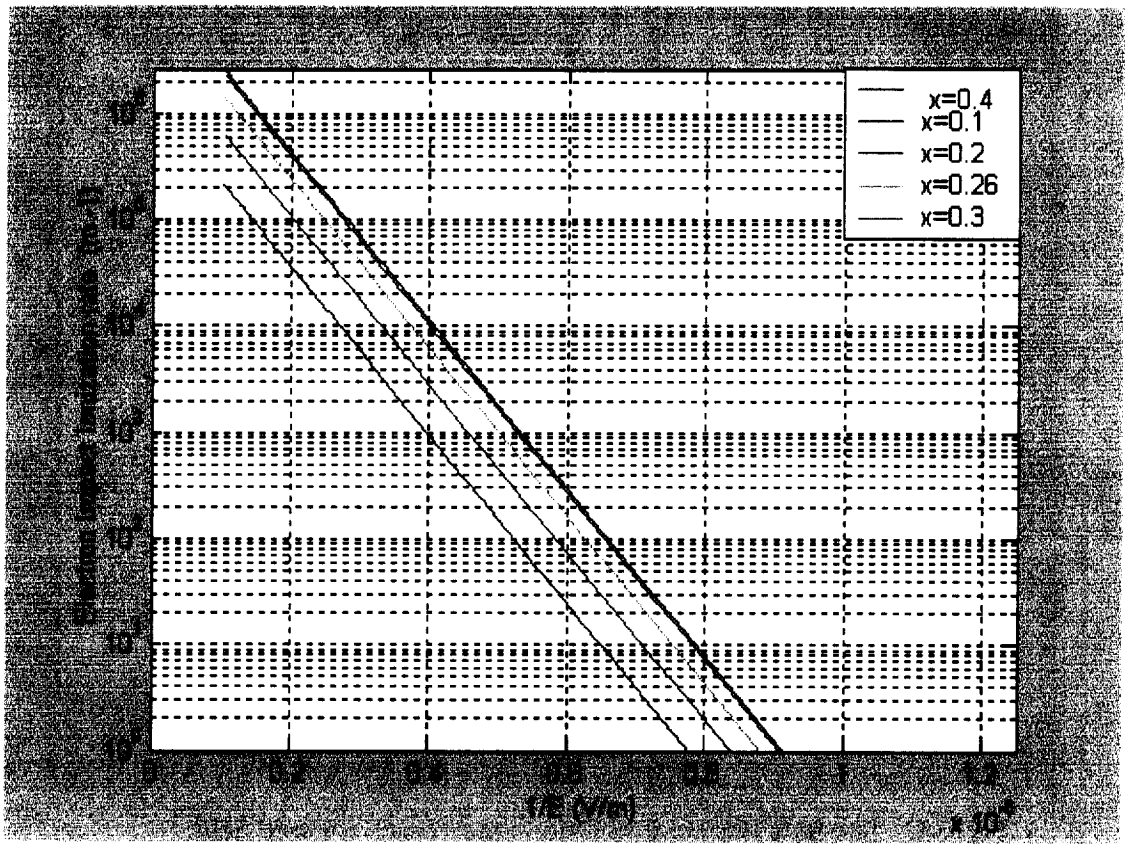

Fig. 36. The electron impact ionization rate versus inverse of electric field.

ionization coefficient (α) changes by a factor k (β/α), and equals 2.1 for the given composition of Al in AlGaAsSb for the existing NASA detector.

Figs. 33 and 34 show the calculations for electric field vs ionization coefficient for holes. The electric field dependence of the electron ionization coefficient α is shown in Figs. 35-36. Both the E vs α and 1/E vs α graphs [26] are plotted for convenience. Since the impact coefficient varies with alloy composition, a set of possible Al compositions in AlGaAsSb, has been used. As seen from the graphs, the increase in composition increases the electron impact ionization rate, for the same applied electric field.

Calculations of multiplication factor [27] for the AlGaAsSb diode are shown in the following graphs. As seen from Figs. 37-40 the multiplication factor, M, increases with increasing Al composition x in the AlGaAsSb material for a given applied voltage. The

multiplication factor also increases with the applied voltage for the fixed composition. These results clearly show that the alloy composition is also an important parameter, and should be carefully considered in the design of a good avalanche photo-detector for this 2 μm application.

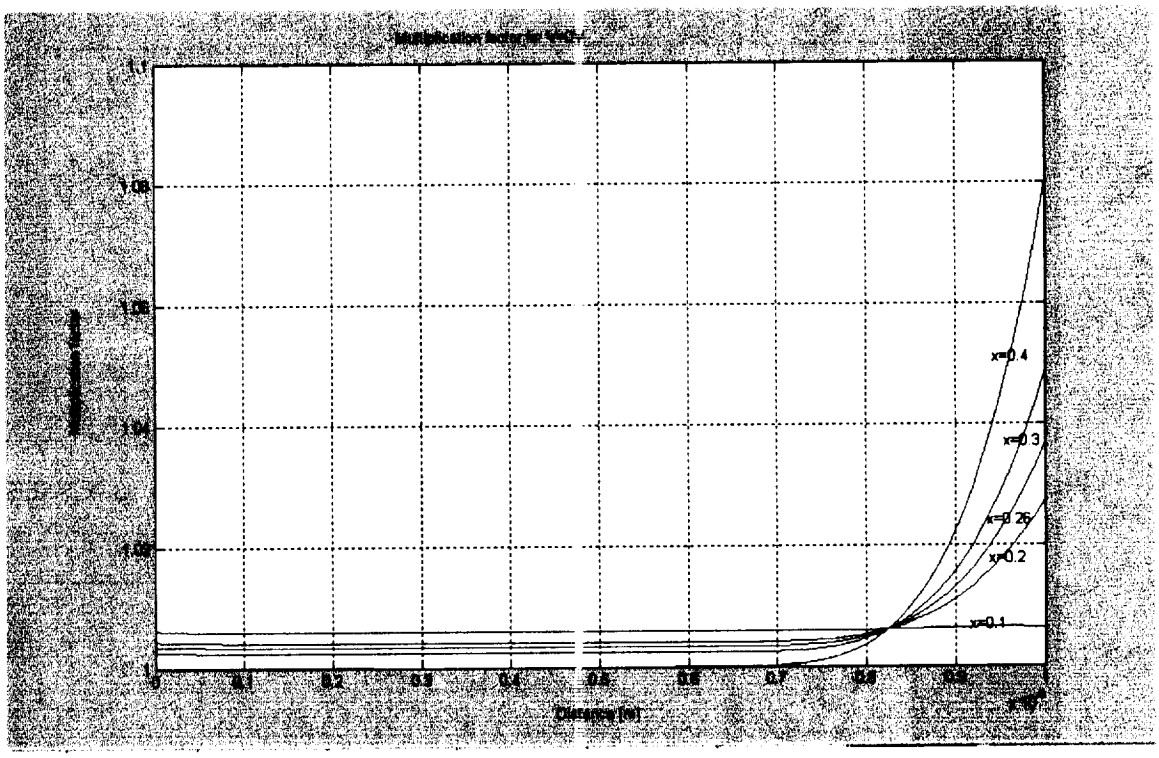

Fig. 37. The variation of multiplication factor with alloy composition at V = 0V.

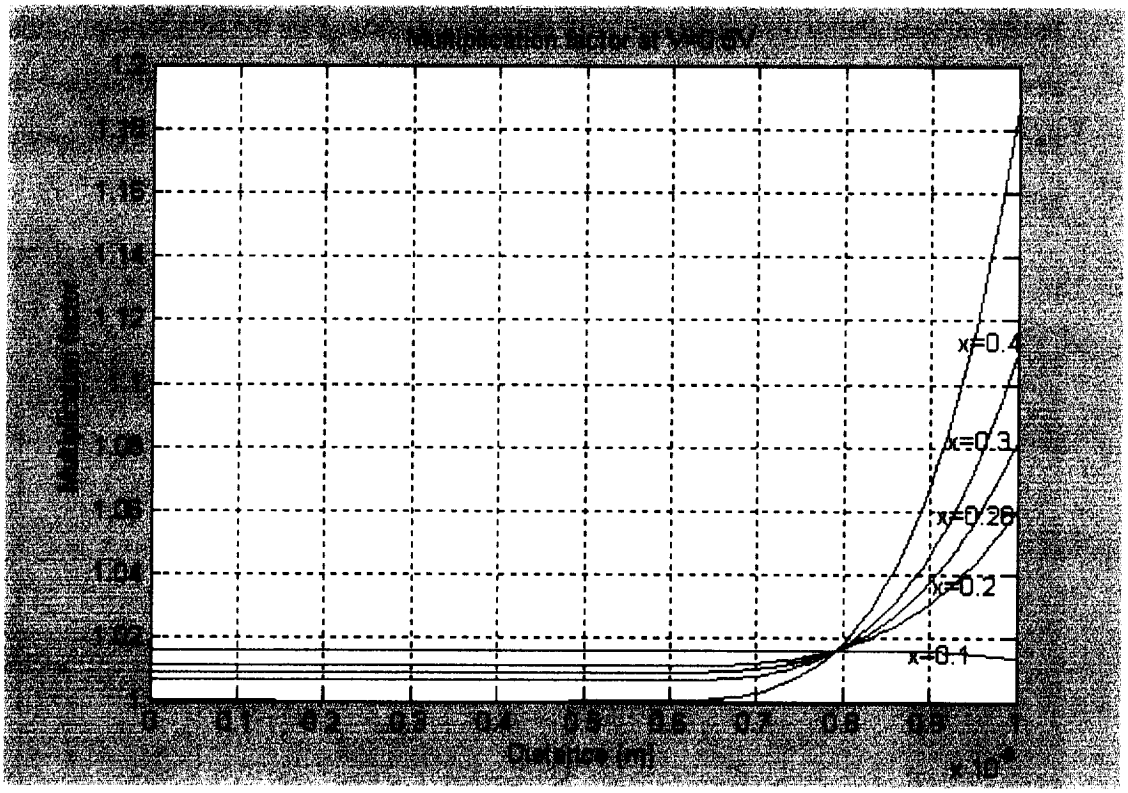

Fig. 38. The variation of multiplication factor with alloy composition at V = 0.5V.

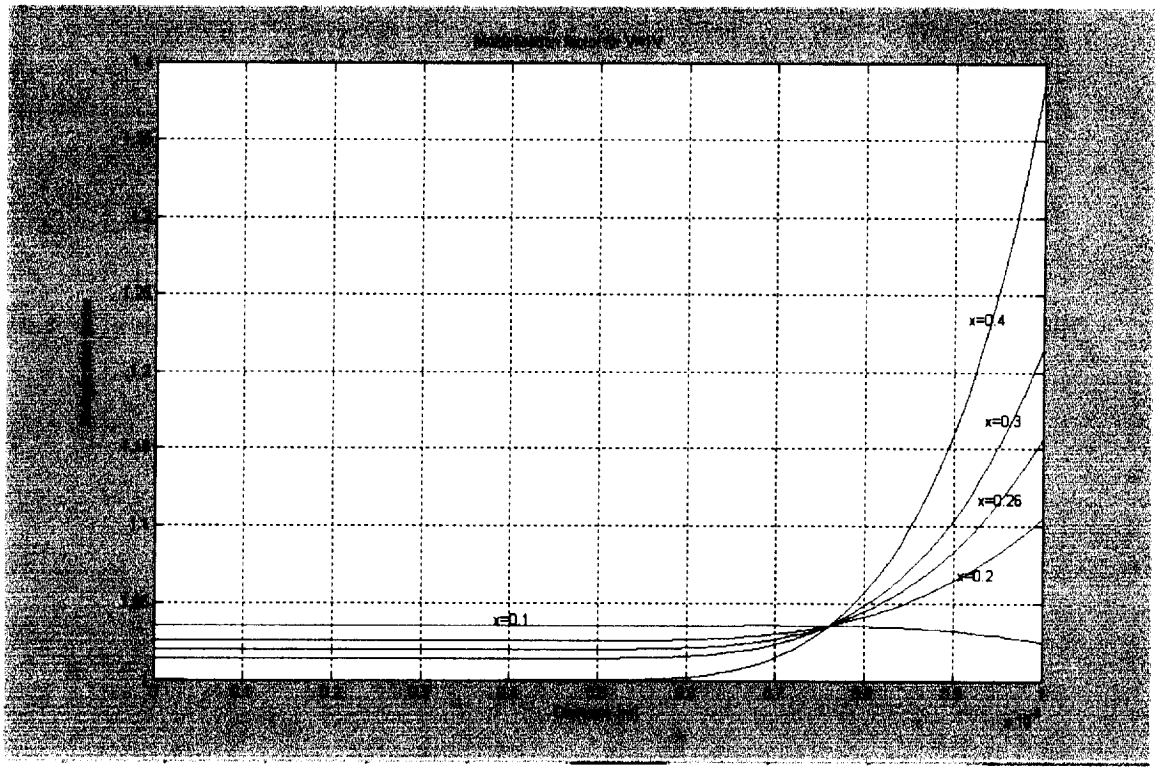

Fig. 39. The variation of multiplication factor with alloy composition at V = 1V.

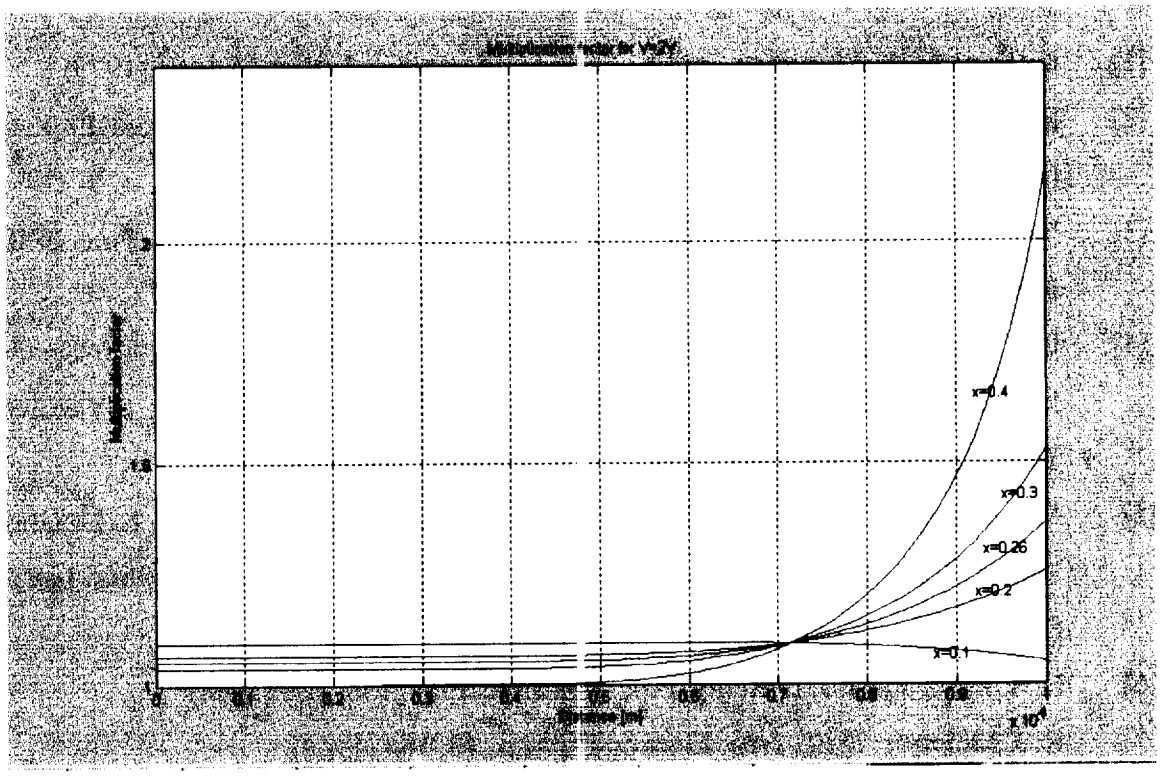

Fig. 40. Variation of multiplication factor with alloy composition at V = 2V.

REFERENCES

[1]. K. Taguchi, Y. Masumato, and K. Nishida, Electronics Letters **15,** 453 (1979).

[2]. E. Tournie, J. L. Lazzari, F. Pitard, C. Alibert, A. Joullie, B. Imbert, J. Appl. Phys. **68,** 5936 (1990).

[3]. Y. P. Yakovlev, A. N. Baranov, A. N. Imenkov, and M. P. Mikhaiolova, Proc. SPIE. **1510,** 170 (1991).

[4]. I. A. Andreeev, M. A. Afrailov, A. N. Baranov, S. G. Konnnikov, M. A. Mirsagatov, M. P. Mikhaiolova, O. V. Salata, V. B. Umanskii, G. M. Filaretova, and Yu. P.Yakolvev, Sov. Tech. Phys. Lett. **15**, 232 (1989).

[5]. M. Mebarki, H. Ait-Kaci, J. L. Lazzari, C. Segura-Fouillant, A. Joullie, L. Llinares, and I. Salesse, Umanskii, G. M. Filaretova, and Yu. P. Yakolvev, Sov. Tech. Phys. Lett. **15**, 253 (1989).

[6]. R. S. Fyath and J. J. O'Reilly, Proc. Inst. Elec. Eng. **135**, 109 (1988).

[7]. R. J. McIntyre, IEEE Tran. Electron Devices. **13**, 164 (1966).

[8]. A. S. Tager, Sov. Phys. Solid State. **8**, 1919 (1965).

[9]. N. R. Howard, J. Electron. Contr. **13**, 537(1962).

[10] R. L. Batdorf, A. G. Chynoweth, G. C. Dacey, and P. W. Foy, J. Appl. Phys. **31,** 1153 (1960).

[11]. A. Goetzberger, B. McDonald, R. H. Haitz, and R. M. Scarlett, J. Appl. Phys. **34,** 1591 (1963).

[12]. K. M. Johnson, IEEE Tran. Electron Devices. **12**, 55 (1965).

[13]. C. A. Lee, R. L. Batdorf, W. Wiegmann, and G. Kaminsky, IEEE Tran. Electron Devices **13**,175 (1996).

[14]. C. Hu, K. A. Anselm, B. G. Streetman, and J. C. Campbell, Appl. Phys. Lett. **69,** 3734 (1996).

[15]. S. D. Personick, Bell Syst. Tech. J. **52,** 843 (1973).

[16]. I. A. Andreev, M. A. Afrailov, A. N. Baranov, and M. P. Mikhailova, Pis'Ma V

Zhurnal Tekhnicheskoi Fizika **16**, 27 (1990).

[17]. M. A. Afrailov, A. N. Baranov, A. P. Dmitriev, M. P. Mikhailova, Y. P. Smorchkova, I. N. Timchenko, V. V. Sherstnev, Y. P. Yakovlev, I. N. Yassievich, Fiz. Tekh. Poluprovodn **24**, 1397 (1990).

[18]. R. A. Garnham, M. D. Learmouth, J. J. Rimington, A. S. M.Ali, M. J. Robertson, and W. A. Stallard, Electronics Letters, **24**, 1416 (1988).

[19]. M. Astles, H. Hill, A. J. Williams, P. J. Wright, and M. L. Young, J. Electronic Materials, **15**, 41(1986).